Cell Reports

Article

A mesenchymal to epithelial switch in Fgf10 expression specifies an evolutionary-conserved population of ionocytes in salivary glands

Graphical abstract

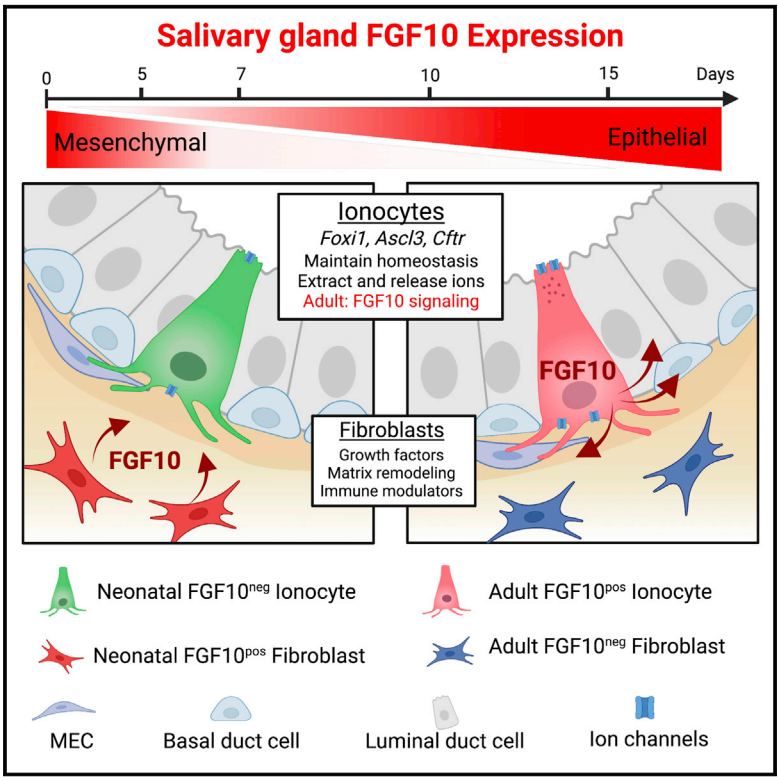

Highlights

- Unique FGF10-expressing ionocytes have been identified within salivary gland ducts
- The FGF10^{pos} ionocytes express the hallmark of ancient ionocyte signature genes
- FGF10 expression shifts from fibroblasts to ionocytes between postnatal days 7 and 15
- Salivary gland ionocytes maintain ion homeostasis and act as niche cells

Authors

Olivier Mauduit, Marit H. Aure, Vanessa Delcroix, ..., Mohammad K. Hajihosseini, Matthew P. Hoffman, Helen P. Makarenkova

Correspondence

hmakarenk@scripps.edu (H.P.M.), mhoffman@nih.gov (M.P.H.)

In brief

Mauduit et al. identified unique FGF10-expressing ionocytes in salivary glands. FGF10 expression shifts from fibroblasts to epithelial ionocytes during postnatal development. Ionocytes play a dual role in salivary gland homeostasis; they maintain specific ion composition in saliva and act as niche cells, providing growth factor support for other epithelial cells.

Mauduit et al., 2022, Cell Reports *39*, 110663
April 12, 2022
https://doi.org/10.1016/j.celrep.2022.110663

CellPress

Cell Reports

CellPress
OPEN ACCESS

Article

A mesenchymal to epithelial switch in Fgf10 expression specifies an evolutionary-conserved population of ionocytes in salivary glands

Olivier Mauduit,[1,7] Marit H. Aure,[2,7] Vanessa Delcroix,[1] Liana Basova,[1] Amrita Srivastava,[1] Takeshi Umazume,[1] Jacqueline W. Mays,[3] Saverio Bellusci,[4] Abigail S. Tucker,[5] Mohammad K. Hajihosseini,[6] Matthew P. Hoffman,[2,7,8,*] and Helen P. Makarenkova[1,7,8,9,*]

[1]Department of Molecular Medicine, The Scripps Research Institute, La Jolla, CA 92037, USA
[2]Matrix and Morphogenesis Section, National Institute of Dental and Craniofacial Research, National Institutes of Health, Bethesda, MD 20892, USA
[3]Oral Immunobiology Unit, National Institute of Dental and Craniofacial Research, National Institutes of Health, Bethesda, MD 20892, USA
[4]Cardio-Pulmonary Institute (CPI) and Department of Pulmonary and Critical Care Medicine and Infectious Diseases, Universities of Giessen and Marburg Lung Center (UGMLC), The German Center for Lung Research (DZL), Justus-Liebig University Giessen, 35392 Giessen, Germany
[5]Centre for Craniofacial and Regenerative Biology, King's College London, London WC2R 2LS, UK
[6]School of Biological Sciences, University of East Anglia, Norwich NR4 7TJ, UK
[7]These authors contributed equally
[8]Senior author
[9]Lead contact
*Correspondence: hmakarenk@scripps.edu (H.P.M.), mhoffman@nih.gov (M.P.H.)
https://doi.org/10.1016/j.celrep.2022.110663

SUMMARY

Fibroblast growth factor 10 (FGF10) is well established as a mesenchyme-derived growth factor and a critical regulator of fetal organ development in mice and humans. Using a single-cell RNA sequencing (RNA-seq) atlas of salivary gland (SG) and a tamoxifen inducible *Fgf10*^{CreERT2}*:R26-tdTomato* mouse, we show that FGF10^{pos} cells are exclusively mesenchymal until postnatal day 5 (P5) but, after P7, there is a switch in expression and only epithelial FGF10^{pos} cells are observed after P15. Further RNA-seq analysis of sorted mesenchymal and epithelial FGF10^{pos} cells shows that the epithelial FGF10^{pos} population express the hallmarks of ancient ionocyte signature *Forkhead box i1 and 2* (*Foxi1*, *Foxi2*), *Achaete-scute homolog 3* (*Ascl3*), and the cystic fibrosis transmembrane conductance regulator (*Cftr*). We propose that epithelial FGF10^{pos} cells are specialized SG ionocytes located in ducts and important for the ionic modification of saliva. In addition, they maintain FGF10-dependent gland homeostasis via communication with FGFR2b^{pos} ductal and myoepithelial cells.

INTRODUCTION

Saliva production by salivary glands (SGs) is critical to lifelong oral health, neutralization of acids for maintenance of oral and dental integrity, and digestion. SGs are composed of pairs of parotid glands (PGs), submandibular glands (SMGs), and sublingual glands (SLGs), and although saliva is produced by acinar cells, its ionic composition is critically modified by duct cells to ensure that saliva is hypotonic, carries neutral pH, and is saturated with calcium and phosphate ions. The SG duct system consists of intercalated ducts (IDs), which directly connect to acini; basally folded striated ducts (SDs); and excretory ducts (EDs) that channel saliva into the oral cavity. The cellular composition of SG ducts is complex and heterogeneous, including a multitude of tuft cells (Sato and Miyoshi, 1997), *Ascl3*-expressing cells (Bullard et al., 2008), EGF-expressing cells (Ono Minagi et al., 2017; Thulesen et al., 2002), and progenitor populations. However, the identity of cells that sense/modify the ionic composition of saliva to make homeostatic adjustments, remains unknown.

As with most glandular organs, the prenatal development of SGs is heavily influenced by fibroblast growth factors (FGFs), a family of 22 signaling molecules that regulate multiple cell behaviors—from cell proliferation, differentiation, and migration to cell fate. FGFs work mainly via paracrine modes by activating one of four membrane-anchored FGF receptors (FGFRs 1-4) with the cooperation of cofactors, such as sulfated proteoglycans, to augment intracellular signaling cascades and changes in gene expression or cytoskeletal remodeling. During SG development, FGF10, and its receptor, FGFR2b, are important, as genetic deletion of either gene in mice causes SG aplasia (Jaskoll et al., 2005). In humans, mutations in *FGF10* or *FGFR2* cause the syndromes—LADD (lacrimo-auriculo-dento-digital) and aplasia of lacrimal and SGs (Entesarian et al., 2007; Mikolajczak

et al., 2016; Milunsky et al., 2006; Shams et al., 2007)—showing that FGF10/FGFR2b signaling is critical to human SG development.

The importance of FGF10 for developmental organogenesis has suggested that it may be a useful factor for regenerative therapies in adult tissues (Lee et al., 2015; Zheng et al., 2015). During SG regeneration in a murine duct ligation injury model, both *Fgf10* and *Sox9* were upregulated (Chatzeli et al., 2017). However, the normal function of FGF10 in adult SGs is largely unknown.

Here, we used lineage-tracing strategies, single-cell RNA sequencing (scRNA-seq) analysis, and analysis of sorted FGF10-expressing ($FGF10^{pos}$) cells to delineate the identity and putative functions of these cells in mouse SGs. We discovered an unexpected switch of FGF10 expression during the second postnatal week from mesenchymal cells to epithelial duct cells. Furthermore, the adult epithelial $FGF10^{pos}$ population resembles *Ascl3*-expressing ($ASCL3^{pos}$) duct cells (Bullard et al., 2008; Rugel-Stahl et al., 2012) and expresses molecular signatures that are characteristic of an ancient ionocyte cell type found in fish and frog, conserved into mouse and human (Chen et al., 2017, 2019; Hsu et al., 2014; Trayer et al., 2015). Importantly, $FGF10^{pos}$ cells highly express *Cftr*, which is critical for exocrine secretion (Noel et al., 2008; Shin et al., 2016; Yokoyama et al., 2019; Zeng et al., 2017). We propose that, in adult SGs, epithelial $FGF10^{pos}$ cells are SG ionocytes with an additional function of maintaining gland homeostasis by paracrine signaling to FGFR2b-expressing cells, including myoepithelial, luminal, and basal ductal cells.

RESULTS

Divergence of *Fgf10* expression in discrete cell populations in early postnatal and adult SGs

The importance of FGF10 in development led us to hypothesize that it plays an uncharacterized but critical role in maintaining gland homeostasis and/or regeneration in adults. As an entry point, we mined a recently published scRNA-seq SMG atlas to identify potential $Fgf10^{pos}$ cell clusters in postnatal and adult glands (Hauser et al., 2020).

The atlas includes neonatal (postnatal day 1 [P1]) and two adult stages (P30 and P300). For our analysis, we used integrated data from all stages, divided into two subsets: P1 and adult (P30 and P300 together). At P1, *Fgf10* was detected in stromal cells (Figure 1A). In the adult, however, an additional $Fgf10^{pos}$ duct population was evident (Figure 1B). These cells co-expressed the well-known duct marker *Ascl3* as well as ion channel transcriptional regulator *Foxi1* (Figure 1B; Data S1), as confirmed by *in situ* hybridization (Figure 1C). There was robust *Fgf10* expression in neonatal stromal cells (440 cells, 12.8% of total). However, the adult stromal population only consisted of 16 cells, 0.5% of the cells in the library (Figure S1A). Furthermore, *Fgf10* expression was detected only in two adult stromal cells from one of the two adult stages and therefore the scRNA-seq data suggest that adult stromal $Fgf10^{pos}$ cells are rare (Figure S1B).

To further interrogate the abundance, distribution, and identity of postnatal and adult $FGF10^{pos}$ cells, we visualized and lineage traced them using $Fgf10^{CreERT2}$:$Rosa26^{tdTomato}$ mice (Figures 1D and 1E), since the field lacks effective anti-FGF10 antibodies for *in vivo* study. The $Fgf10^{CreERT2}$:$Rosa26^{tdTomato}$ mice were treated with tamoxifen (TM), allowing constitutive expression of tdTomato (TOM) in $FGF10^{pos}$ cells and their descendants (Figures 1D and 1E). TM administration at day P4/5 (analyzed at P20), resulted in TOM expression exclusively in stromal cells near the secretory acini and ducts (Figure 1E, white arrowheads), while reporter induction at P28/29 (analyzed at P40 and P60) did not show any TOM^{pos} stromal cells. Instead, a large number of luminal epithelial cells, identified as cytokeratin-19-positive ($Krt19^{pos}$) cells were detected (Figure 1F). Flow cytometry analysis confirmed that all TOM^{pos} labeled at P4/5 cells lack EpCAM expression (Figure 1G), while TOM^{pos} cells labeled at adult stage (36/37) have an epithelial identity, as they express EpCAM (Figure 1H). These findings confirm that FGF10 expression continues postnatally, emerging in a discrete large population of adult duct cells.

The compartmental switch in *Fgf10* expression is stable and correlates with duct maturation

The intriguing compartmental switch in *Fgf10* expression from mesenchymal to epithelial cells suggests a correlation with new developmental event/function. Therefore, to define the time frame of this switch we carried out TM injections at closer time-intervals during postnatal development (Figure 2A). TM treatment at P4/5 resulted in labeling of stromal cells exclusively (Figure 2B), while TM treatment between P7 and P11 resulted in labeling of both stromal (Figures 2C and 2D, white arrowheads) and epithelial cells (Figures 2C and 2D, yellow arrows). In contrast, TM administration at or after P15, yielded only epithelial TOM^{pos} cells (Figure 2E).

Quantification of TOM^{pos} cells revealed a steady reduction of $FGF10^{pos}$ cells in the stroma, followed by a steady increase in epithelial $FGF10^{pos}$ cells (Figure 2F). These changes could be interpreted as either some stromal $FGF10^{pos}$ cells undergoing mesenchymal to epithelial transition (MET) and migrating into the epithelium, or stromal cells switching off FGF10 expression or dying, accompanied by induction of FGF10 expression in duct cells. To resolve these two possibilities, we induced Cre-mediated recombination at P4/5 and lineage traced cells for an extended period, analyzing cells at P20, P60, P120, and P210 (Figures 2G and 2H). We found that, labeled at P4/5, stromal TOM^{pos} cells remain stromal at all time periods (Figures 2G and 2H), suggesting that they endure late into adulthood but that expression of FGF10 in these cells is switched off (also see graphical abstract). Alternatively, TM was injected into young adult mice at P28/29 and cells were traced for 8 months. We found that the labeled TOM^{pos} cells remained ductal throughout this period of time (Figure 2I), while no mesenchymal $FGF10^{pos}$ cells were detected, indicating that P28/29-derived $FGF10^{pos}$ duct cells are self maintained and/or long lived (see graphical abstract).

Since sexual dimorphism has been noted in murine SMGs, we quantified and compared the abundance of labeled $FGF10^{pos}$ duct cells in males versus females. For this analysis, 3-month-old adult mice were injected with TM for two subsequent days and epithelial ($EpCAM^{pos}$:TOM^{pos} and $EpCAM^{pos}$:TOM^{neg}) cells were quantified by flow cytometry 1 week after

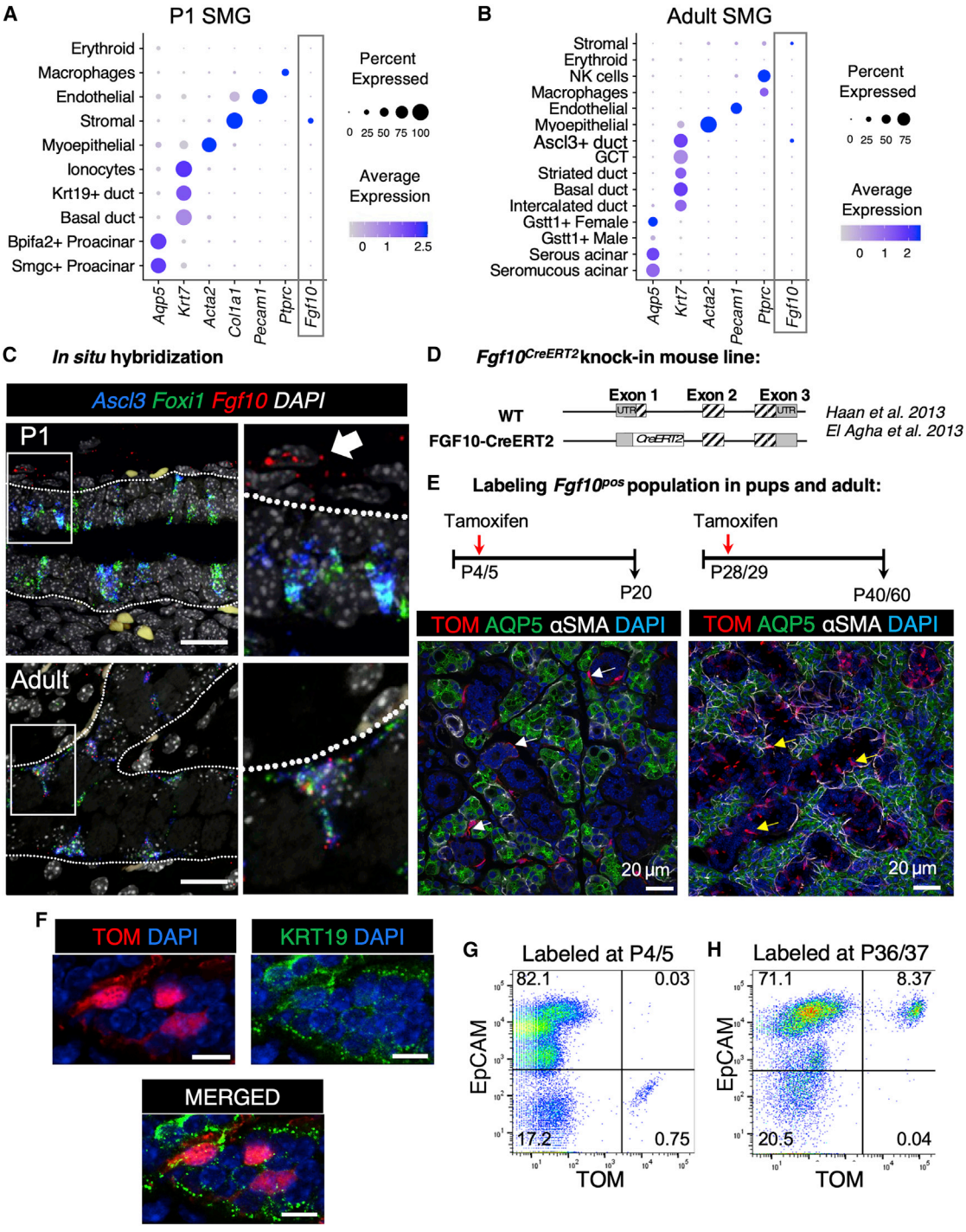

Figure 1. *Fgf10* expression in postnatal SMGs

(A) SMG scRNA-seq data showed *Fgf10* expression in stromal cells at birth.

(B) In adult SMGs, *Fgf10* was expressed within the *Ascl3*+ cluster by scRNA-seq.

(C) *In situ* hybridization at P1 confirmed co-expression of *Ascl3* (blue) and *Foxi1* (green) in duct cells, while *Fgf10* (red) was detected in stromal cells (insert, arrow). In adult SMGs, *Fgf10*, *Foxi1*, and *Ascl3* are co-expressed in duct cells. Dotted lines indicate the basement membrane. Scale bars, 10 μm.

(D) *Fgf10*^{CreERT2} mouse schematic.

(E) Immunostaining of SMG cryosections with AQP5 (acinar marker, green) and αSMA (MEC marker, gray). After induction at P4/5, FGF10^{pos} cells (red, white arrowheads) were stromal, located in close association with acini. After TM treatment at P28/29, FGF10^{pos} cells (red, yellow arrows) were found within ducts.

(F) TOM^{pos} duct cells express KRT19. Scale bars, 10 μm (G–H). Flow cytometry analysis of SMG cells 1 week after TM treatment of (G) pups or (H) adults stained with EpCAM antibody. See also Figures S1 and S2, Data S1 and S3.

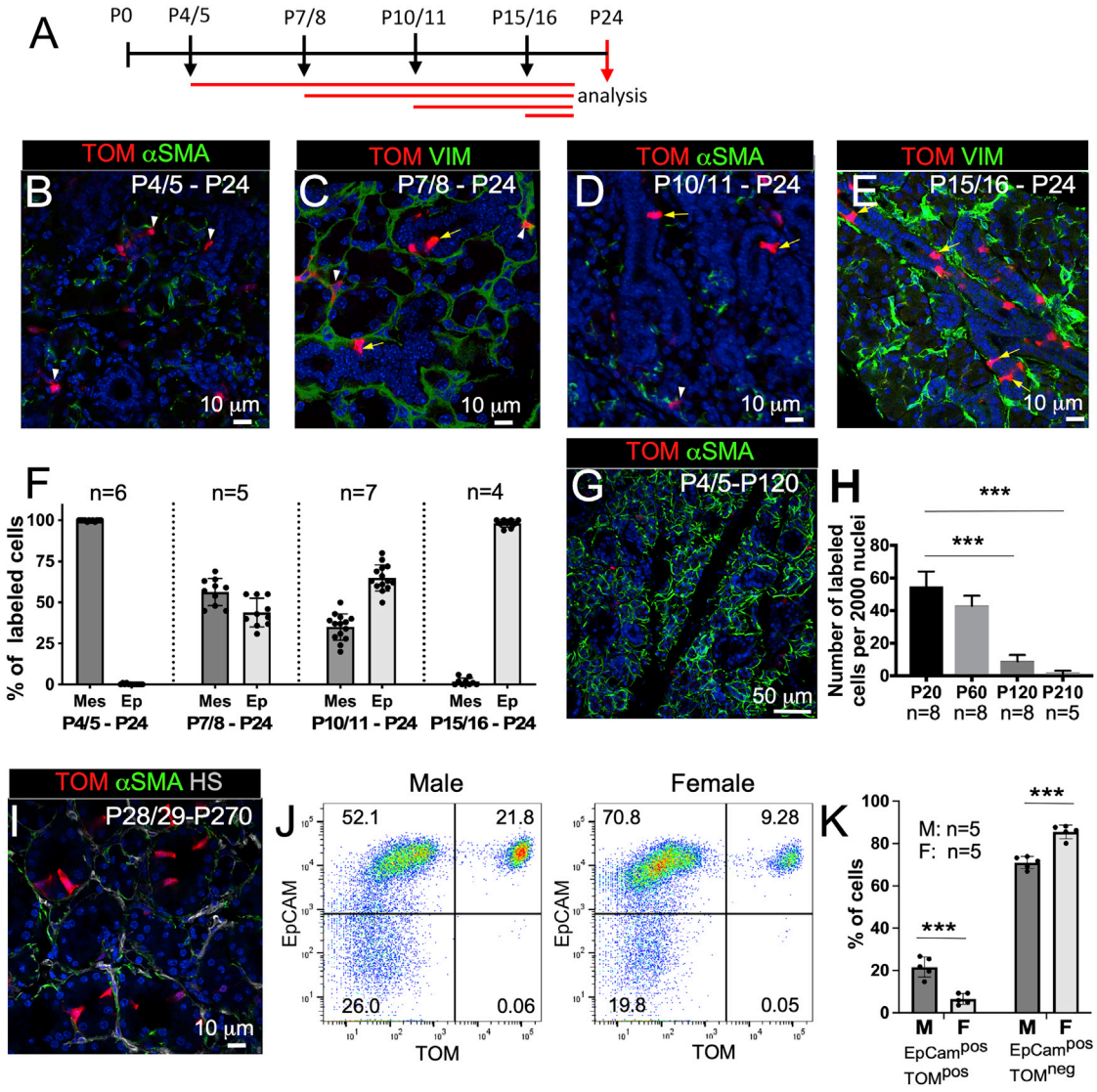

Figure 2. FGF10 expression switches to SMG epithelium during postnatal development

(A–F) (A) Experimental timeline: TM was administrated at P4/5 (B), P7/8 (C), P10/11 (D), and P15/16 (E) and analyzed at P24. (F) Quantification of TOM^{pos} cells in the epithelium (Ep) and mesenchyme (Mes).

(G and H) Lineage tracing of FGF10^{pos} (TOM^{pos}) cells labeled at P4/5. Cells labeled at P4/5 remain stromal (G) and their numbers decrease with time (H).

(I) FGF10^{pos} (TOM^{pos}) cells labeled at P28/29 remain epithelial (cells were analyzed at P270).

(J and K) FACS analysis and quantification of percentage of FGF10^{pos} (TOM^{pos}) cells in males and females. Adult, 3-month-old mice were injected with TM and SMGs were dissociated and stained with EpCAM antibody after 1 week. All bar plots are mean ± SD; unpaired t test (***$p < 0.001$; n, number of mice). See also Figures S2 and S3, and Data S3.

the first TM injection. Females had significantly fewer FGF10^{pos} (EpCAM^{pos}:TOM^{pos}) cells than males (around 22% of total cells in males versus 7% in females) (Figures 2J and 2K), consistent with reports that male SMGs have significantly more ducts than females (Pardini and Taga, 1996). Interestingly, the percentage of other epithelial cells (EpCAM^{pos}:TOM^{neg}) was higher in females (Figures 2J and 2K).

Combined, these findings suggest that MET is an unlikely explanation for emergence of FGF10^{pos} duct cells. Rather, FGF10 is switched on *de novo* in the epithelial compartment. Since duct maturation in mouse SMGs starts around P10 (Durban et al., 1994), these findings also suggest that the compartmental switch signifies functional maturation of a subset of duct cells.

The neonatal and early postnatal FGF10^{pos} cells are stromal fibroblasts

To characterize *Fgf10*^{pos} stromal cells during early postnatal development, we analyzed the scRNA-seq data from the P1 SMGs. We identified 1,504 significant genes in *Fgf10*^{pos} cells compared with all other cells. Among the top 60 genes, were several well-characterized fibroblast markers: collagens

(*Col3a1*, *Col1a1*); the small leucine-rich proteoglycans (*Lum*, *Bgn*, *Dcn*); and *Pdgfra* (Figures S2A and S2B; Data S2), suggesting that these cells are fibroblasts. A variety of immune modulators, including *Rarres2*, *Serpinf1*, *Cxcl12*, and *Ccl11*, were also enriched (Figures S2A and S2B).

Although few adult fibroblasts were present in the scRNA library, the transcriptional profile overlapped with that of P1 cells (Figures S1C, S2A, and S2B). As expected, *Fgf10*^{pos} cells at P1 were *Cdh1* negative (Figures S2C and S2D) and vimentin (*Vim*, mesenchymal marker) positive (Figure S2D), which was confirmed by overlapping staining of vimentin (VIM) and TOM^{pos} cells after TM induction (Figure S2E). In contrast to adult glands, all TOM^{pos} cells were E-cadherin (ECAD) positive and VIM negative (Figure S2F).

To further dissect the transcriptional profile and functional role of stromal and epithelial FGF10^{pos} cell populations, we labeled cells in the *Fgf10*^{CreERT2}*:Rosa26*^{tdTomato} mice by TM administration at P4/5 and P59/60 and sorted TOM^{pos} cells by FACS and bulk RNA-seq, which allows deeper interrogation of transcription compared with scRNA-seq. Significantly up- and downregulated genes were identified based on a Log2-fold change (Log2FC) of +1.5 or −1.5, respectively, and a false discovery rate corrected p value of 0.05 or less. We identified a total of 1,498 differentially expressed genes with 406 upregulated genes and 1,092 downregulated genes in epithelial TOM^{pos} cells of adult SMGs compared with the TOM^{pos} cells isolated from SMGs of pups.

In support of the scRNA-seq data, stromal TOM^{pos} cells were fibroblasts and had significantly enriched expression of genes involved in the cell cycle, in particular the M-phase (Figure S3; Data S3), suggesting that FGF10^{pos} fibroblasts proliferate. They also expressed higher levels of metalloproteinases (*Mmp9/12/14/15/27*) and metalloproteinase-disintegrins (ADAM and ADAMTS family proteins), suggesting they are involved in ECM degradation and tissue morphogenesis. Accordingly, we also noted a higher expression of ECM components (collagens, laminin, tenascin, versican), but also an enrichment of pathways related to signal transduction (“integrin pathway,” “ERK signaling,” “phospholipase-C pathway”) (Data S3). The TOM^{pos} fibroblasts also expressed growth factor receptors *Fgfr1*, *Fgfr2*, *Igf1r*, and *Erbb4*, and ligands *Fgf10*, *Fgf12*, *Fgf18*, and *Igf2*. Taken together, the gene expression profile suggests that stromal *Fgf10*^{pos} cells are proliferating fibroblasts that are involved in ECM remodeling and likely communicate with epithelial, endothelial, and immune cells.

Duct FGF10^{pos} cells bear molecular hallmarks of evolutionary-conserved ionocytes

Analysis of scRNA-seq from adult SMGs determined that *Fgf10* is expressed in cells labeled by the transcription factor *Ascl3*. Although this duct population has previously been reported (Arany et al., 2011; Bullard et al., 2008), its specific functional role is not clear and transcriptome analysis of these cells had not been performed.

The transcription factors *Foxi1* and *Foxi2* were among the highly enriched and specific genes (Figures 3A, 3B, and 3C; Data S2 and S4; Table S1). *Foxi1* is a master regulator of various ion channels and proton pumps. Like the scRNA-seq, bulk RNA-seq of cells sorted from adult SMG TOM^{pos} cells showed that epithelial FGF10^{pos} cells express *Ascl3*, *Foxi1*, *Foxi2*, and *Stap1* (Tables S2 and S3). *Stap1* is suggested to function as an adaptor molecule downstream of KIT receptor (Masuhara et al., 2000) and previously, KIT was shown to overlap with NKCC1 (Takeyama et al., 2015), a known marker for acinar and ASCL3^{pos} cells in the mouse SMGs (Arany et al., 2011).

Recently, these genes were described as characterizing an evolutionarily conserved type of cells called ionocytes (Hsu et al., 2014; Martin et al., 2019; Montoro et al., 2018; Shono et al., 2011). We compared transcriptional profile from the scRNA-seq SG atlas with rare cell types found in the airways, including pulmonary neuroendocrine cells, brush cells, and ionocytes (pulmonary scRNA-seq, GSE102580). This showed a significant overlap between SG cells and pulmonary ionocytes (Figure 3D). Overlapping genes included canonical ionocyte markers, such as the transcription factors *Ascl3*, *Foxi1*, *Cttnbp2*, and *Sox4*, and channels and transporters including *Cftr*, *Slc12a2*, and *Kcnma1* (Figures 3B and 3C; Data S4 and S5). The Cl^- channel CFTR was also reported within the SG SDs of humans (Zeng et al., 2017; Zinn et al., 2015). In addition to *Cftr*, we identified the HCO_3^- transporter *Slc4a11* (Table S2), which is the most abundant Slc4 family member in SGs (Yang et al., 2019). SGs from *Slc4a11*$^{-/-}$ mice have less duct area and show a significant decrease of *Ascl3* expression in addition to impaired NaCl reabsorption (Yang et al., 2019). We also detected most subunits of *H*$^+$*-ATPase* (V-ATPase-subunit genes: *Atp6v1c2* and *Atp6v0d2*) (Data S4) in addition to multiple transporters (Table S2). V-ATPases are generally involved in proton transport across the plasma membrane as well as vesicle trafficking and are involved in modifying saliva in SG ducts (Sahara et al., 2015).

Gene enrichment analysis also suggested that potential functions of FGF10^{pos} cells include ECM-receptor interactions, the renin-angiotensin system, phagosome function, endocrine and other factor-regulated calcium reabsorption, collecting duct acid secretion, gastric acid secretion, metabolic pathways, oxidative phosphorylation, and cyclic AMP signaling (Figure 3E).

Although the cluster of *Ascl3*^{pos} cells identified at P1 consisted of few cells (14 cells, 0.4% of total), the transcriptional profile was similar compared with the adult *Ascl3*^{pos} population, suggesting that the establishment of ionocyte gene expression profiles occurs by birth, while *Fgf10* expression is unique to the adult population (Figures 3B and 3C).

Fgf10^{CreERT2}*;Rosa26*^{tdTomato} mice are used to label FGF10^{pos} (TOM^{pos}) cells, allowing immunostaining of ionocyte markers found by RNA-seq. As expected, TOM^{pos} cells in ducts costained epithelial ECAD and ductal marker KRT7 (Figure 4A). TOM^{pos} cells also costained ASCL3, FOXI1, NKCC1 (*Slc12a2*), and CFTR (Figure 4A). Both basolateral NKCC1 and apical CFTR staining (Figure 4A) suggest specialization in ion secretion. TOM^{pos} cells were found in the granular convoluted tubules (GCT) (red arrows) and SDs (yellow arrows) but not in the IDs (Figure 4B, white arrowheads).

Next, we asked whether molecular parallels were found in ionocytes of the human SGs. Using the Human Protein Expression Atlas (https://www.proteinatlas.org/), we found similar expression of ASCL3 (Figures S4A and S4B) and FOXI1 (Figures S4C and S4D), which were enriched in a subset of cells within the

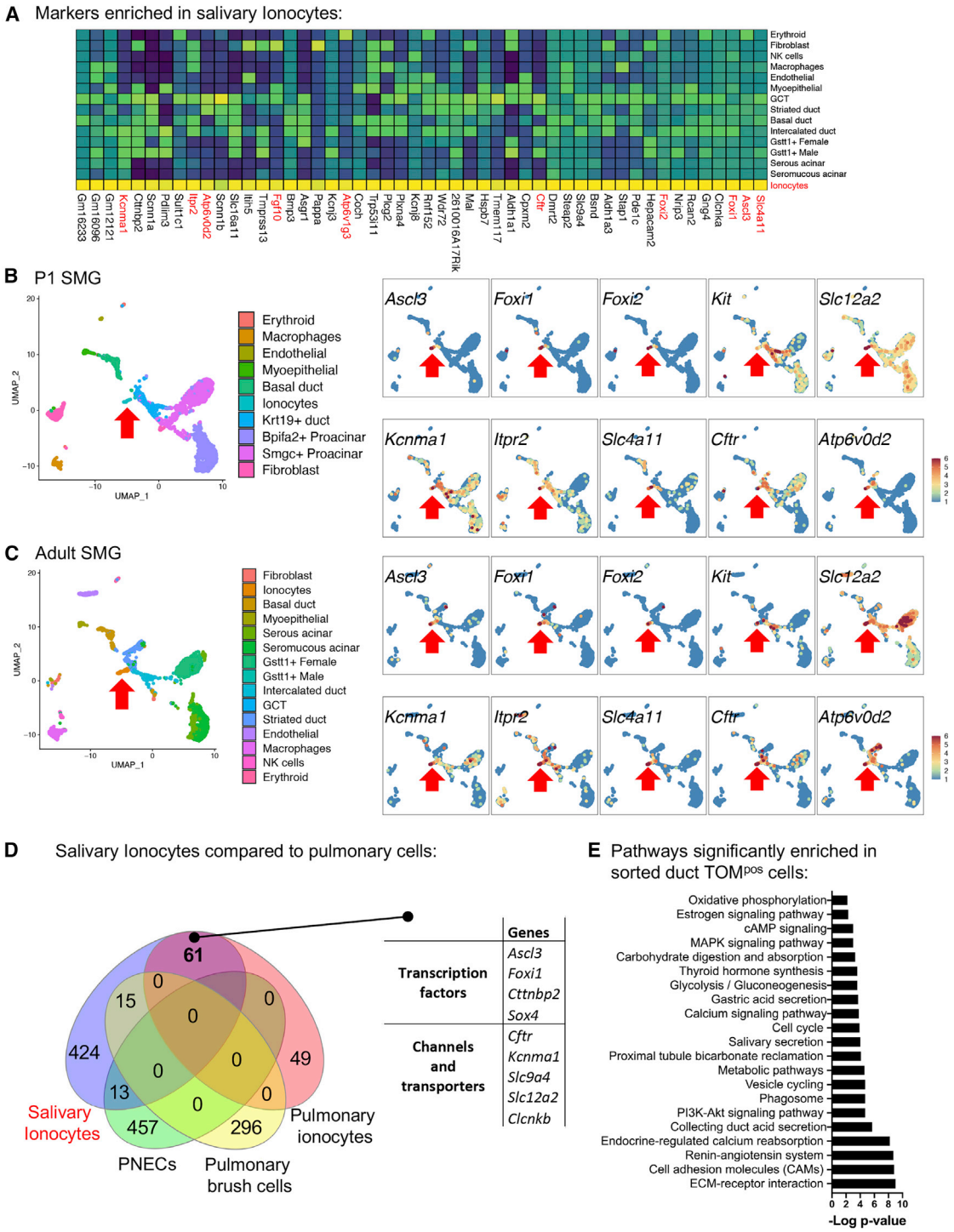

Figure 3. Pathways and genes significantly enriched in adult Fgf10^{pos} SG ionocytes

(A) Heatmap showing average expression of the top 50 enriched genes defining SG ionocytes. Canonical ionocyte genes are in red.

(B and C) UMAPs of P1 (B) and adult (C) SMGs indicating expression of canonical ionocyte genes and known markers of duct subpopulations.

(D) Comparison of enriched genes in SG ionocytes with PNECs, pulmonary brush cells, and pulmonary ionocytes shows significant overlap. Overlapping genes include key transcription factors and channels/transporters.

(E) Pathways and gene expression analysis in FGF10^{pos} cells (adult P60 compared with postnatal P7). Pathway analysis based on bulk RNA sequencing of isolated adult FGF10^{pos} cells compared with mesenchymal FGF10^{pos} cells. See also Figure S4, Table S1, Data S2, S4, and S5.

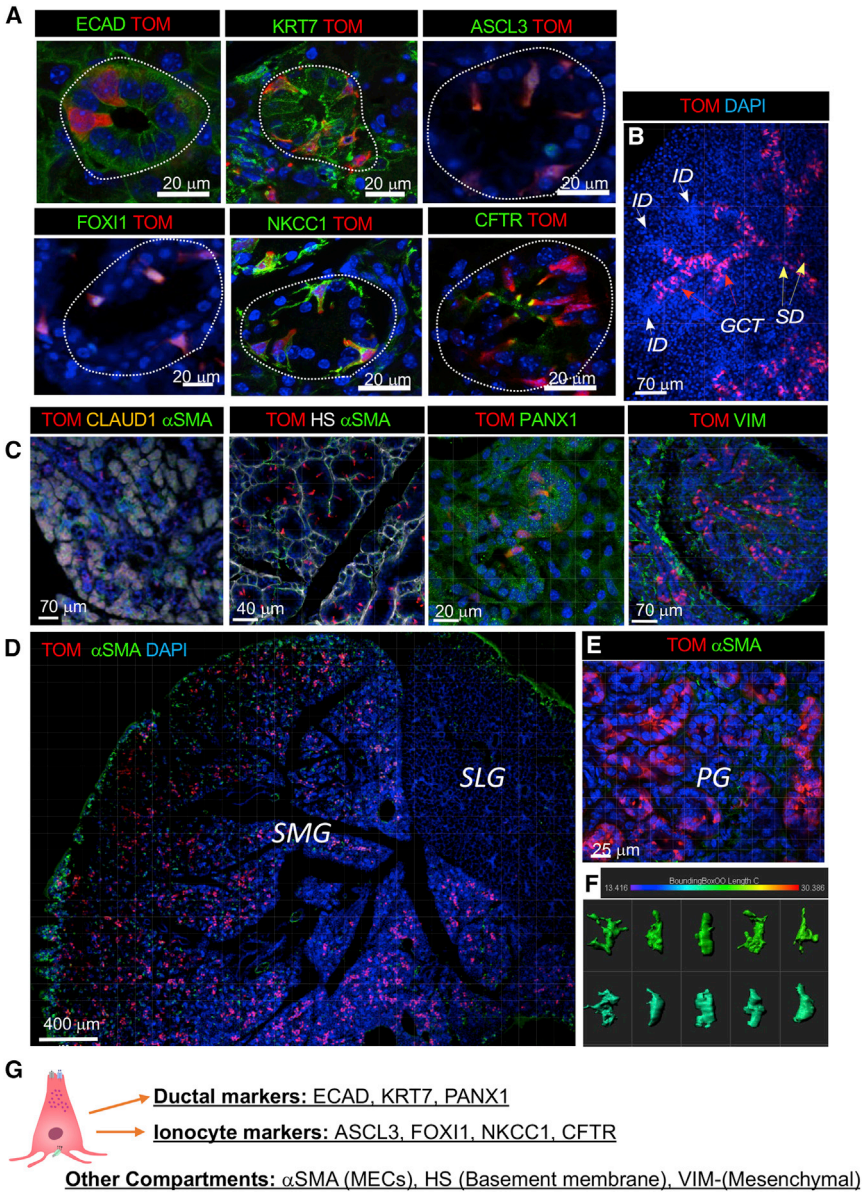

Figure 4. In adult SMGs and PGs, FGF10^{pos} cells are restricted to the ED, SD, and GCT ducts and express ionocyte markers

(A) In adult glands, FGF10^{pos} cells (TOM, red) express E-cadherin (ECAD, green), KRT7 (green), ASCL3 (green), FOXI1 (green), NKCC1 (green), and CFTR (green), which are expressed at the apical membrane of FGF10^{pos} cells. Nuclei labeled with DAPI (blue).

(B) In adult SMG FGF10^{pos} cells (TOM, red) were found in the GCTs (red arrows) and SDs (yellow arrows) but not in the IDs (white arrows).

(C) FGF10^{pos} cells were labeled at P29/30 (TOM, red) and stained with different antibodies. Acini were labeled with claudin (orange); MECs were labeled with αSMA (green); the basement membrane was labeled with heparan sulfate (HS) (gray); ducts were labeled with pannexin-1 (PANX1); stromal cells were labeled with VIM (green); nuclei labeled with DAPI (blue).

(D and E) FGF10^{pos} cells (TOM, red) were found within ducts of SMGs (D) and PGs (E), while not in SLGs (D). FGF10^{pos} cells were detected only within the mesenchyme.

(F) IMARIS bounding box software was used to analyze shape and size of FGF10^{pos} cells.

(G) Summary of immunostaining used to label different cell types and gland compartments. Also see Figures S4 and S5, Data S6.

SDs of human SG, while ATP1B1 and ATP6V1C2 were expressed in all SDs (Figures S4E–S4I).

Taken together, the gene and protein expression profiles of ASCL3^{pos}/FGF10^{pos} epithelial cells confirm that these cells are a specialized population of SG ionocytes with potential roles in acid-base homeostasis. Moreover, SG ionocytes share conserved transcriptional profiles with a variety of ionocyte types found in different animal phyla.

SMG and PG FGF10^{pos} ionocytes have distinctive pyramidal cell morphology with extensive basal filopodia

Having established a strong molecular correlation between FGF10 expression and ionocyte identity, we next analyzed their distribution and shape. Analysis of the TOM^{pos} cells combined with immunostaining with markers of different gland compartments, such as claudin-1 (acinar marker), heparan sulfate (basement membrane marker), pannexin-1 (duct and acinar marker), VIM (mesenchymal marker), and α-smooth muscle actin (αSMA) (myoepithelial [MEC] cell marker), clearly showed FGF10^{pos} cells within the GCT, SDs and EDs (not shown), and not in acini or IDs, in adult SMGs (Figures 4B and 4C). Furthermore, labeled epithelial cells were found in both SMGs (Figure 4D, SMG) and PGs (Figure 4E, PG), while in the SLGs we only detected TOM in a small number of stromal cells (Figure 4D, SLG). Although ASCL3^{pos} cells have been reported in all major SGs (Bullard et al., 2008), surprisingly the FGF10^{pos}/ASCL3^{pos} ionocytes were found only in the SMGs and PGs (Figures 4D and 4E).

We also analyzed a different transgenic *Fgf10*^{LacZ} (Fgf10$^{Mlc1v\text{-}nLacZ\text{-}v24}$) reporter line (Hajihosseini et al., 2008) to validate observations made in the *Fgf10*^{CreERT2}*:Rosa26*^{tdTomato} mouse. X-gal staining of SMG sections were identical to our previous findings, confirming that FGF10^{pos} cells are found in ducts, while in SLGs FGF10^{pos} cells were only found in the mesenchyme (Figures S5A and S5B). Immunostaining of SMG sections with β-galactosidase (β-Gal) antibody detected numerous β-Gal^{pos} cells (Figure S5C; β-Gal^{pos} cells are green) in GCT, SD, and ED. We also did not detect any mesenchymal FGF10^{pos} cells in SMGs, further supporting that FGF10 expression switches from fibroblasts to epithelial ionocytes.

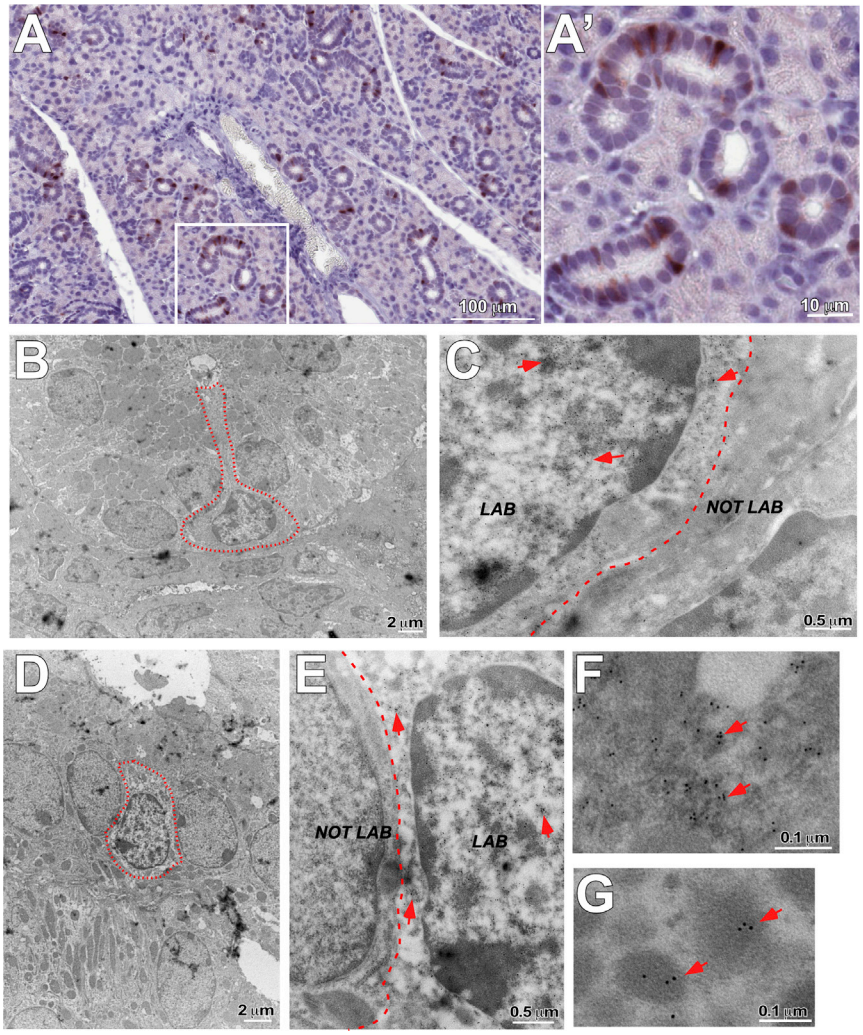

Figure 5. Ultrastructure of SG ionocytes

TM was injected at the P28/29 and SMGs were analyzed at P60. Electron microscopic sections of SMGs were labeled with the antibody against dsRed coupled to 6 nm colloidal gold particles.

(A and A') (A) Immunostaining of paraffin section using dsRed antibody that recognizes RFP and tdTomato (Clontech) specifically labeled a subset of cells (brown) in GCT; (A') insert showing enlarged area (white square) in (A).

(B–G) Transmission electron micrographs of female (B and C) and male SMGs (D–G). Labeled cells (B and D) (outlined by red dotted line) had a pyramidal shape, with distinctive nuclear and cytoplasm ultrastructure. Cells had basally located nuclei with electron-dense material near the nuclear membrane. (C and E–G) High magnification of cells labeled with gold particles (labeled cell [LAB], aggregates of gold particles marked by red arrows) in (C and F) and not labeled (NOT LAB) adjacent neighbor cells. (F and G) High magnification of labeled cell showing gold particles within cytoplasm and small granules.

Cell morphology is an important characteristic that distinguishes different cell types. The majority of TOM^{pos} ionocytes had narrow apical and wide basal parts, referred to as a pyramidal morphology (Figures 4A and S5D). The basal part of the ionocytes often had numerous thin cell processes similar to filopodia, penetrating the basement membrane (Figure S5E, see insert). We scanned large areas of SMG sections (Figure S5E) and found that the apico-basal length of most ionocytes ranges between 15 and 25 μm (17.7 ± 3.1 μm) and that their volume ranged between 250 and 400 μm^3 (330.1 ± 60.5 μm^3) (Figures 4F and S5F). The basal filopodia extend along the duct, indicating that ionocytes can directly contact multiple cells non-adjacent to them (Figures 4G, S5D, and S5E, insert).

Next, we performed immunostaining (Figure 5A, A') with anti-dsRed that recognizes TOM to confirm the specificity of the staining pattern of FGF10^{pos} cells (Figure 5A, A'). We then performed immunogold labeling of electron microscopic sections (Figures 5B–5F) using this antibody. This confirmed the SG ionocyte's morphology and revealed a distinctive ultrastructure with basal nuclei and cells containing inclusions of electron-dense material (Figures 5B–5E). The cytoplasm did not contain many granules (Figures 5B–5F). Immunogold labeling was detected in the cytoplasm, small granules, and nuclei of these cells (Figures 5C, 5E, 5F, and 5G, LAB [labeled cell], red arrows) but not in neighboring cells (Figures 5C and 5E, NOT LAB [not labeled cell]) or control sections omitting primary antibody (not shown). Taken together, this characteristic cell morphology is identical to that reported for SG tuft cells, which are described at the ultrastructural level as having a narrow apex that protrudes in the lumen with apical microvilli and a basally placed nucleus with narrow projections toward the basal lamina (Sato et al., 1998; Sato and Miyoshi, 1988).

FGF10^{pos} ionocytes are predicted to act as support cells

The transcriptome of SG ionocytes suggests a major role in ion secretion and saliva modification; however, FGF10 expression also suggests an additional role as niche cells. Thus, we identified ionocyte-enriched ligands and receptors in the adult SMG scRNA-seq data using an adapted version of a large-scale map of cell-cell interactions (Ramilowski et al., 2015, 2016). Several ligands and receptors in addition to *Fgf10* were significantly enriched in adult ionocytes, as shown in a dot plot (Figure 6A). Ligands, such as *App*, *Gnas*, and *Pkm*, were enriched but were not specific, indicating that these are more general connections between many cell types in the gland (Figure 6A). Furthermore, the list of enriched receptors included *Pvr*, *Slc16a2*, *Pgrmc1*, *Kit*, *Fxyd6*, *Atp6ap2*, *Npr1*, *Plxna4*, and *Aplp2*. However, their potential ligands/interactions were not detected in the dataset and thus not included in further analysis. We performed a ligand-receptor analysis to find potential

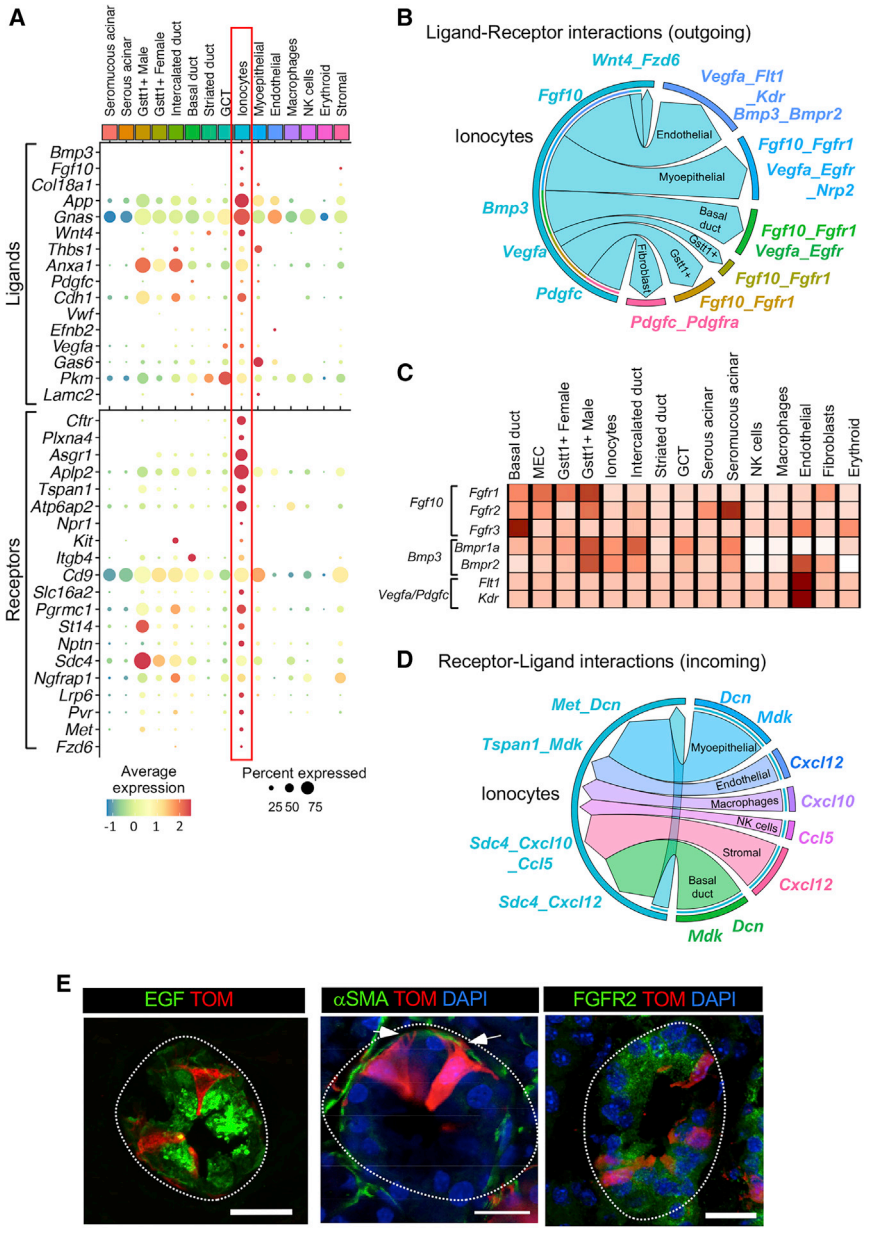

Figure 6. SG ionocytes are predicted to act as support cells

(A) DotPlot showing ligands and receptors significantly enriched in adult SG ionocytes.

(B) Interaction analysis identified potential outgoing signals from ionocytes to endothelial, MECs, basal ducts, Gstt1+ ducts, and fibroblasts, as well as ionocytes. Highlighted in the chord diagram are some of these interactions through the secreted ligands *Fgf10*, *Wnt4*, *Bmp3*, *Vegfa*, and *Pdgfc*.

(C) Heatmap showing average expression of known receptors of *Fgf10*, *Bmp3*, and *Vegfa* and *Pdgfc* in adult SMGs as detected by scRNA-seq.

(D) Interaction analysis predicts incoming signals based on enriched receptors in ionocytes. Highlighted here are signals coming from MECs, basal ducts, and endothelial and immune cells.

(E) Ionocytes in close contact with EGF^{pos} (green) and FGFR2^{pos} (green) duct cells and αSMA^{pos} MECs (green, white arrows). Ducts are outlined by white dotted lines. Scale bars, 20 μm. See also Figure S6 and Data S6.

interactions to and from ionocytes using the enriched ligands and receptors (Data S6). In general, the highest number of potential interactions were found between ionocytes and basal duct cells, MECs, endothelial cells, and macrophages for both outgoing and incoming interactions.

The enriched expression of both the ligand *Wnt4* and receptor *Fzd6* in ionocytes suggests autocrine Wnt signaling (Figures 6A and 6B). Ionocytes were also enriched for the growth factors *Vegfa* and *Pdgfc* (Figures 6A and 6B). Both growth factors may interact with epithelial and non-epithelial cells via *Egfr*, *Nrp2*, *Flt1*, *Kdr*, and *Pdgfr*, as shown in the chord plot (Figure 6B). The analysis also indicated interactions between ionocytes and endothelial, MEC, basal, and Gstt1^{pos} duct cells through *Bmp3* and *Fgf10* (Figure 6B). *Bmp3* can interact with several receptors, including BMPR2 and BMPR1a; and, although both receptors were detected in the dataset, only *Bmpr2* in endothelial cells met the criteria for the interaction analysis (Figure 6B). Both receptors are found in several duct populations as well as acinar and endothelial cells (Figure 6C). *FGF10* can bind FGFR1 and -2 (Jaskoll et al., 2002, 2005; Makarenkova et al., 2009; Zinkle and Mohammadi, 2019) but not FGFR3 (Jacky et al., 2013). Although only *Fgfr1* expression level was significant, *Fgfr1*, *Fgfr2*, and *Fgfr3 were* enriched in basal duct cells, a subset of IDs and MECs (Figures 6B and 6C). This suggests that FGF10^{pos} cells in adult SMGs may signal in a paracrine fashion to other duct cells and MECs.

Among the incoming signals from basal cells and MECs were ligands that bind to *Met* and *Tspan1*, both involved in growth, motility, and cell migration. In addition, ionocytes may interact with other epithelial cells and macrophages through *Syndecan 4* (*Sdc4*), a heparan sulfate proteoglycan that functions as a receptor for intracellular signaling and can interact with the chemokines *Cxcl12*, *Cxcl10*, and *Ccl5*, all involved in SG disease (Blokland et al., 2021) (Figure 6D).

Taken together, our analysis predicts that, beyond their functional role in acid-base homeostasis of saliva, ionocytes act as supporting cells for duct cells (such as EGF- and FGFR2b-expressing cells) and MECs, with which they directly interact (Figure 6E, white arrows). Thus, we hypothesized that SG ionocytes may regulate cell growth or plasticity of cells that they interact

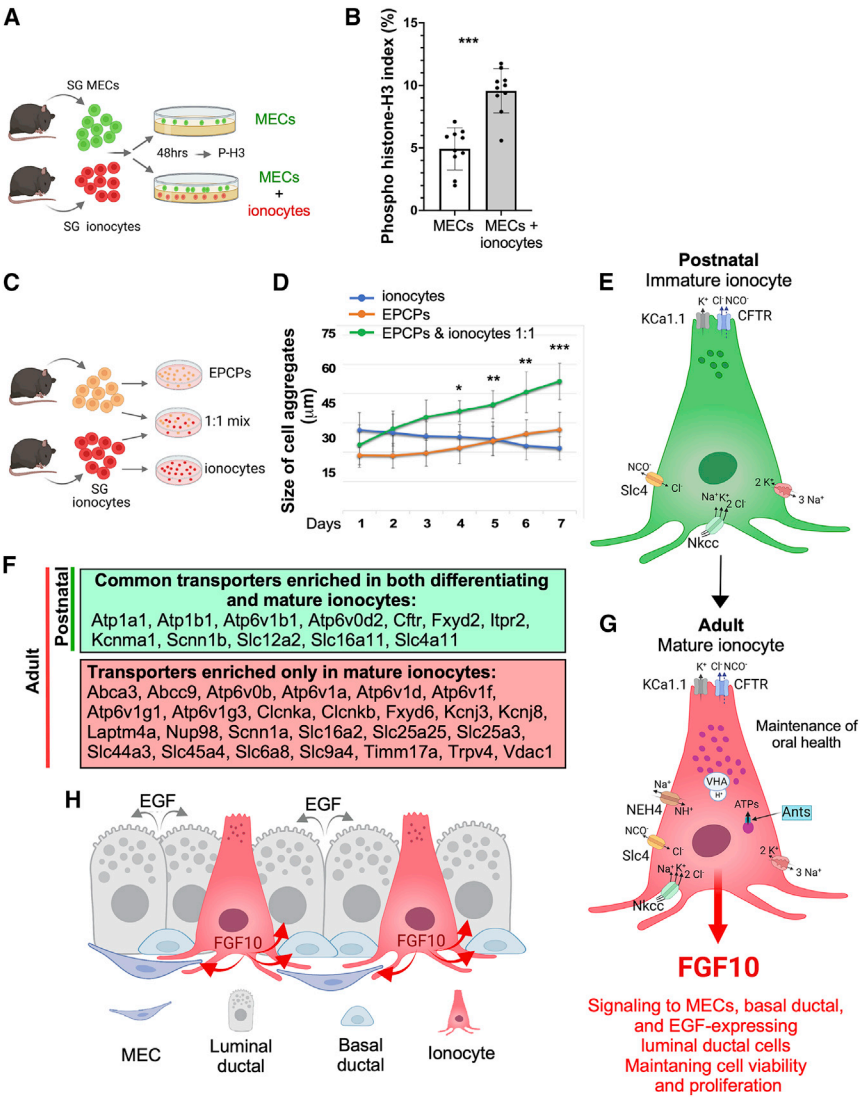

Figure 7. SG FGF10^{pos} ionocytes maintain growth of epithelial cells and saliva homeostasis

(A) Experimental setup: SG FGF10^{pos} ionocytes were isolated from the *Fgf10^{CreERT2}:R26-tdTomato* mice, and SG MECs from the αSMA-GFP mice. Matrigel mixed with or without ionocytes was spread on a glass-bottomed dish and MECs were plated on top. After 48 h culture, cells were immunostained with P-H3 antibody (proliferation marker) and DAPI. P-H3^{pos} nuclei within MECs were quantified.

(B) Plots (mean ± SD) comparing the proportion of proliferating cells in control (MECs, n = 10) and experimental (MECs + ionocytes, n = 10) conditions (n, number of replicates). Statistical significance was assessed with an unpaired t test (***p < 0.001).

(C) Experimental setup: lacrimal EPCPs and SMG FGF10^{pos} cells were isolated and grown *in vitro* either alone (controls) or mixed in a 1:1 ratio.

(D) Isolated SMG FGF10^{pos} ionocytes increase growth of lacrimal gland epithelial cell progenitors (EPCPs). Cells reaggregate and their size was measured from 1 to 7 days (40–50 aggregates per each condition/time point; mean ± SD, two-tailed Fisher's exact test; *p < 0.05, **p < 0.01, ***p < 0.001).

(E) Schematic of ionocyte prior to induction of *Fgf10* expression. Neonatal *Ascl3^{pos}* cells in SMGs are not fully differentiated and express fewer ion transporter genes.

(F) List of common and unique transporters between developing and mature ionocytes.

(G) Schematic showing differentiated SMG ionocytes where active Na^+ absorption is likely driven through the NHE4 (*Slc9a4*), NKCC1 (*Slc12a2*), and Na+/K+-ATPases (*Atp1a1* and/or *Atp1b*) in the basolateral membrane creating passive Cl^- transport. Secretion is driven by Cl^- and NCO^- secretion through CFTR and other Cl^- channels in the apical membrane. Active Cl^- secretion creates Na^+ and water movement across the epithelium paracellularly and/or transcellularly.

(H) Function of FGF10 in SG duct epithelium. FGF10^{pos} ionocytes signal to FGFR2b^{pos} cells, such as basal duct, MEC, and EGF^{pos} cells in a paracrine fashion. FGF10 released from ionocytes maintain cell viability and plasticity. Models were created using Biorender. All bar plots are presented as mean ± SD.

with. Therefore, we set out to test whether ionocytes could support the growth of other epithelial cells.

SG ionocytes support the growth of other epithelial cells

To directly test whether ionocytes can support the growth of SMG epithelial cells they interact with, we sorted TOM^{pos} ionocytes from the SMG of *Fgf10$^{CreERT2/+}$:R26-tdTomato$^{fl/f}$* mice and MECs from the SMGs of αSMA-GFP mice (Zyrianova et al., 2019). MECs were cultured for 48 h on top of a thin layer of Matrigel with or without ionocytes (Figure 7A). At the end of the culture period, cells were stained with histone-3-phospho (P-H3) antibody to quantify proliferating cells. A significant increase in P-H3^{pos} cells was observed in MECs cocultured with ionocytes (Figure 7B), supporting our hypothesis that FGF10^{pos} ionocytes act as niche cells for MECs.

To date, multipotent stem cells have not been definitely identified or isolated from SGs (Rocchi et al., 2021). However, we previously isolated adult lacrimal gland epithelial cell progenitors (EPCPs) that express FGFR2b and are located in the basal duct compartment of the lacrimal gland (Basova et al., 2020; Gromova et al., 2017). Therefore, we isolated EPCPs from the lacrimal gland (Gromova et al., 2017) and TOM^{pos} ionocytes from SGs by FACS (Figure 7C). Sorted SMG TOM^{pos} ionocytes of *Fgf10$^{CreERT2/+}$:R26-tdTomato$^{fl/fl}$* mice were mixed with EPCPs in a 1:1 proportion and allowed to grow in reaggregated cultures for 7 days as described previously (Gromova et al., 2017). Purified ionocytes and purified EPCPs were used as controls. We found that control EPCP reaggregates increased 30% in size, while control ionocyte reaggregates survived but did not increase (Figure 7D). By contrast, the size of the reaggregates containing both EPCPs and FGF10^{pos} ionocytes almost doubled by day 7 (Figure 7D). Together, these experiments suggest that SG ionocytes can support and maintain growth of adult epithelial cells *in vitro*.

DISCUSSION

We identified and characterized a unique FGF10^{pos} epithelial population of ionocytes in the duct compartments of mouse SMGs and PGs, with cellular and molecular parallels in man and fish. The transcriptome included *Foxi1*, *Foxi2*, *Cftr*, *Slc12a2*, and *Kcnma1*, which are canonical markers for ionocytes and conserved across species. When further dissecting the transcriptional profile and morphology of these cells, we found that they overlap with several previously described but poorly defined SG duct subpopulations that had been named according to individual marker expression or morphology. For example, *Ascl3*^{pos} cells that co-express both *Slc12a2* and *Kcnma1* were previously identified as duct progenitors during fetal development (Arany et al., 2011; Bullard et al., 2008). Our analysis of P1 *Ascl3*^{pos} cells suggests they are not fully differentiated as they express fewer transporters than adult *Ascl3*^{pos} ionocytes (Figures 7E–7G). Several reports indicate that GCT subpopulations labeled by *Kit* (Kwak et al., 2018), *Slc4a11* (Roussa et al., 1998), luminal localization of ATPases (Lee et al., 2012), and IP3R2 in "pioneer cells" (Yamamoto-Hino et al., 1998), all express markers enriched in ionocytes. Similarly, several cell populations have been described based on morphology, such as "pillar cells" (Mori et al., 2011) and "Tuft cells" (Sato et al., 1998; Sato and Miyoshi, 1997). We suggest that all these previously described cell types are SG ionocytes.

A critical function of the SG epithelium is to control the volume and electrolyte composition of saliva by sequestering ions so that secreted saliva is hypotonic. The acinar cells secrete isotonic fluid containing NaCl, while ducts modify the volume and electrolyte fluid composition by absorbing the Na^+ and Cl^- and then secreting Cl^- and HCO_3^- (Jirakulsomchok and Schneyer, 1979; Luo et al., 2001; Pirani et al., 1987). The ion transport mechanisms involved in the fluid and electrolyte secretion in SGs maintains oral homeostasis and health. However, it was unclear if specific cell types in the duct were responsible for the ion exchange. The transcriptional profiles of adult SG ionocytes showed expression of the cellular machinery to absorb Na^+ and secrete K^+, Cl^-, and HCO_3^- into saliva (Lee et al., 2012). *Slc4a11*, a member of the Slc4 HCO_3^- transporter family that participates in NaCl reabsorption (Yang et al., 2019) is also enriched in adult SMG ionocytes. The H^+ transporting ATPases (V-ATPases, also known as VHA ATPases)—large multisubunit proton pumps (Holliday, 2012)—are also enriched in adult ionocytes, regulating cellular pH and participating in control of protein degradation, ligand secretion, and receptor recycling (Figures 7F and 7G).

Another important finding here is that ionocytes are highly enriched for CFTR, which mediates Cl^- and HCO_3^- secretion (Lee et al., 2012) and integrates the entire duct transport function at the luminal membrane by interacting with multiple transporters and the cytoskeleton (Short et al., 1998). Expression of CFTR at the apical membrane of the ionocytes provides a mechanism for active secretion similar to one found in mitochondria-rich cell ionocytes of seawater-acclimatized fish (Bodinier et al., 2009; Hsu et al., 2014; Lorin-Nebel et al., 2006). These cells function by the cooperative action of three major ion transport proteins: basolaterally located Na+/K+ ATPase; basolaterally located Na+:K+:2Cl− cotransporter (NKCC); and an apically located Cl channel, homologous to CFTR. In branchial epithelia of fish, this type of ionocyte plays osmoregulatory functions and helps with seawater-to-freshwater transfer (Chang et al., 2013; Takei et al., 2014). Similarly, tetrapod renal tubule ionocytes are indispensable in maintaining systemic salt and water balance (Breves et al., 2014). The SG ionocytes also have a basolateral Na^+:K^+:2Cl^- cotransporter (NKCC1/Slc12A2) (Arany et al., 2011; Jalali et al., 2017), Na+/K+ ATPases, and apical CFTR (Figures 4A, 7E, and 7G). Importantly, dysfunction of CFTR protein leads to several human diseases (Paranjape and Zeitlin, 2008) and increases production of proinflammatory cytokines (Domzalska et al., 2016) that may result in hypofunction and/or xerostomia or dry mouth. In mice, mutations in the *Cftr* gene or a decrease in CFTR expression during disease leads to inflammation, increased fibrosis, and tissue damage. Moreover, restoration of *Cftr* expression partially eliminates inflammation and tissue damage and was sufficient to restore saliva flow (Zeng et al., 2017). Thus, further analysis of ionocyte differentiation and function may provide an important insight into SG disease.

The expression of FGF10 in SG ionocytes suggests additional functions apart from modulating saliva ion concentrations. Interestingly, recombinant FGF10 application stimulates fluid secretion in humans and pig fetal lungs (Meyerholz et al., 2018; Prince, 2018). More specifically, FGF10 increases *Cftr* mRNA expression, lumen expansion, and cell proliferation (Meyerholz et al., 2018). In addition to increasing *Cftr* expression, FGF10 also induces fluid production via an unknown mechanism that increases Cl^- secretion, which is likely to be CFTR independent in the lung (Graeff et al., 1999). Whether FGF10 is able to stimulate Cl^- secretion and fluid production in SGs remains to be determined. However, FGF10 is a multifunctional growth factor that signals to epithelial cells through the FGFR2b and is essential for multi-organ development and tissue homeostasis in adults (Petiot et al., 2003). FGF10 binds to the extracellular matrix avidly and thus likely has a local signaling effect (Izvolsky et al., 2003; Makarenkova et al., 2009; Thotakura et al., 2019). Therefore, target cells for FGF10 signaling need to be close to FGF10-producing cells (Figure 7G). As a pleiotropic factor, Fgf10 can also function cell autonomously within FGF10^{pos} cells, as shown recently in a study of LADD syndrome mutation (Mikolajczak et al., 2016). Our data suggest that FGF10-secreting ionocytes may signal specifically to the MECs and basal duct cells, and possibly to the cells located in the ID that are in close proximity to FGF10-secreting cells (Figure 7H). These cells that potentially directly interact with FGF10^{pos} ionocytes express FGFR2 (Figures 6C and 6E) and retain cellular plasticity throughout the mouse lifespan (Shubin et al., 2020). Interestingly, analysis of FGFR2 expression in male and female human SGs shows that, as in mouse SMGs, this receptor is highly enriched in the basal duct (Figures S6A and S6B) and MECs (Human Protein Atlas: Figures S6A–S6D). We predict that ionocytes may detect gland damage via changes in SG ion composition and secrete FGF10 to enhance epithelial repair and regeneration, although this hypothesis remains to be investigated.

The shift of FGF10 expression from mesenchymal to epithelial cells is intriguing and observed within a very narrow postnatal time frame. The differentiation of duct cells occurs between 1

and 2 weeks after birth (Kurabuchi et al., 2019), which correlates with the timing of the FGF10 expression shift. Differentiation of GCT cells is normally under hormonal control of androgens (dihydrotestosterone) and possibly other hormones (Kurabuchi et al., 2019; Morrell et al., 1987). Mice treated with thyroid hormones and androgens convert SD cells into the GCT-like cells (Kurabuchi, 2006). Whether hormones control the FGF10 expression shift to ionocytes in SGs remains to be determined. The specific timing of epithelial FGF10 expression suggests that it could be either involved in GCT maturation, or required for postnatal duct growth and differentiation. However, further work is needed to distinguish these possibilities.

In summary, FGF10^{pos} SG ionocytes play roles in both saliva ion modification and act as niche cells, providing growth factor support for other epithelial cell growth and differentiation. Ionocytes are located in the duct system and are likely sentinels that can detect cell dysfunction, and potentially coordinate repair and regeneration of the gland via communication with basal duct cells and myoepithelial cells within the gland, both of which have epithelial regenerative potential after gland damage.

Limitations of the study

FGF10^{pos} cells may interact with many types of cells expressing FGFRs in different biological contexts, which remain to be tested. Another limitation is low number of adult fibroblasts in scRNA-seq, which may be a technical issue with dissociation from ECM. We have not directly explored the physiology of the channels in adult ionocytes and in particular the physiology of CFTR, which plays an important role in the repair and regeneration of SG function (Zeng et al., 2017). We have based much of our speculation on the role of these cells in duct ion physiology on gene expression of channels and similar gene regulatory pathways present in other ionocytes.

STAR★METHODS

Detailed methods are provided in the online version of this paper and include the following:

SUPPLEMENTAL INFORMATION

Supplemental information can be found online at https://doi.org/10.1016/j.celrep.2022.110663.

ACKNOWLEDGMENTS

We are grateful to Dr. Malcolm Wood and Dr. Theresa Fassel and the Scripps Research Institute Core Microscopy Facility for performing of immunoelectron microscopy of the SMGs. H.P.M., O.M., V.D., A.S., L.B., and T.U. were supported by the National Eye Institute (NEI), United States, grants 5R01EY026202 and 5R01EY028983, and NIDCR grant R01DE031044. S.B. was supported by the Cardio-Pulmonary Institute and by grants from the Deutsche Forschungsgemeinschaft (DFG) (BE4443/1-1, BE4443/4-1, BE4443/6-1, KFO309 P7, and SFB1213 projects A02 and A04). M.P.H., J.W.M., and M.H.A. were supported by the Intramural Research Program of the National Institute of Dental and Craniofacial Research, NIH. The graphical abstract was created using Biorender.

AUTHOR CONTRIBUTIONS

Conceptualization, H.P.M. and M.P.H.; investigation, H.P.M., O.M., M.H.A., V.D., L.B., A.S., and T.U.; resources, M.K.H., S.B., and A.S.T.; formal analysis, O.M., M.H.A., H.P.M., and M.P.H.; writing – original draft, H.P.M., M.H.A., O.M., and M.P.H.; writing – review & editing, H.P.M., M.P.H., M.H., S.B., O.M., M.H.A., V.D., J.W.M., and A.S.T.; funding acquisition, H.P.M., M.P.H., and M.H.; supervision, H.P.P. and M.P.H.; methodology, M.K.H., J.W.M., and S.B.

DECLARATION OF INTERESTS

The authors declare no competing interests.

INCLUSION AND DIVERSITY

We worked to ensure sex balance in the selection of non-human subjects. While citing references scientifically relevant for this work, we also actively worked to promote gender balance in our reference list.

Received: September 16, 2021
Revised: January 21, 2022
Accepted: March 21, 2022
Published: April 12, 2022

SUPPORTING CITATIONS

The following references appear in the supplemental information: Angerilli et al. (2018); Christensen et al. (2012); Cole et al. (2010); Dave and Kwong (2020); Edlund et al. (2015); Giffen et al. (2019); Horng et al. (2017); Leach and Morrisey (2018); Montoro (2019); Mukherjee et al. (2019); Quigley et al. (2011); Shaughnessy and McCormick (2020); Sun et al. (2018); Vieira Braga et al. (2019); Wang et al. (2019); Zhang et al. (2017).

REFERENCES

Anders, S., Pyl, P.T., and Huber, W. (2015). HTSeq–a Python framework to work with high-throughput sequencing data. Bioinformatics *31*, 166–169.

Angerilli, A., Smialowski, P., and Rupp, R.A. (2018). The Xenopus animal cap transcriptome: building a mucociliary epithelium. Nucleic Acids Res. *46*, 8772–8787.

Arany, S., Catalan, M.A., Roztocil, E., and Ovitt, C.E. (2011). Ascl3 knockout and cell ablation models reveal complexity of salivary gland maintenance and regeneration. Dev. Biol. *353*, 186–193.

Basova, L., Parfitt, G.J., Richardson, A., Delcroix, V., Umazume, T., Pelaez, D., Tse, D.T., Kalajzic, I., Di Girolamo, N., Jester, J.V., et al. (2020). Origin and lineage plasticity of endogenous lacrimal gland epithelial stem/progenitor cells. iScience *23*, 101230.

Blokland, S.L.M., Flessa, C.M., van Roon, J.A.G., and Mavragani, C.P. (2021). Emerging roles for chemokines and cytokines as orchestrators of immunopathology in Sjogren's syndrome. Rheumatology *60*, 3072–3087.

Bodinier, C., Boulo, V., Lorin-Nebel, C., and Charmantier, G. (2009). Influence of salinity on the localization and expression of the CFTR chloride channel in the ionocytes of Dicentrarchus labrax during ontogeny. J. Anat. *214*, 318–329.

Breves, J.P., McCormick, S.D., and Karlstrom, R.O. (2014). Prolactin and teleost ionocytes: new insights into cellular and molecular targets of prolactin in vertebrate epithelia. Gen. Comp. Endocrinol. *203*, 21–28.

Bullard, T., Koek, L., Roztocil, E., Kingsley, P.D., Mirels, L., and Ovitt, C.E. (2008). Ascl3 expression marks a progenitor population of both acinar and ductal cells in mouse salivary glands. Dev. Biol. *320*, 72–78.

Butler, A., Hoffman, P., Smibert, P., Papalexi, E., and Satija, R. (2018). Integrating single-cell transcriptomic data across different conditions, technologies, and species. Nat. Biotechnol. *36*, 411–420.

Chang, W.J., Wang, Y.F., Hu, H.J., Wang, J.H., Lee, T.H., and Hwang, P.P. (2013). Compensatory regulation of Na^+ absorption by Na^+/H^+ exchanger and Na^+-Cl^- cotransporter in zebrafish (Danio rerio). Front Zool *10*, 46.

Chatzeli, L., Gaete, M., and Tucker, A.S. (2017). Fgf10 and Sox9 are essential for the establishment of distal progenitor cells during mouse salivary gland development. Development *144*, 2294–2305.

Chen, X.L., Zhang, B., Chng, Y.R., Ong, J.L.Y., Chew, S.F., Wong, W.P., Lam, S.H., and Ip, Y.K. (2017). Na(+)/H(+) exchanger 3 is expressed in two distinct types of ionocyte, and probably augments ammonia excretion in one of them, in the gills of the climbing perch exposed to seawater. Front Physiol. *8*, 880.

Chen, Y.C., Liao, B.K., Lu, Y.F., Liu, Y.H., Hsieh, F.C., Hwang, P.P., and Hwang, S.L. (2019). Zebrafish Klf4 maintains the ionocyte progenitor population by regulating epidermal stem cell proliferation and lateral inhibition. PLoS Genet. *15*, e1008058.

Christensen, A.K., Hiroi, J., Schultz, E.T., and McCormick, S.D. (2012). Branchial ionocyte organization and ion-transport protein expression in juvenile alewives acclimated to freshwater or seawater. J. Exp. Biol. *215*, 642–652.

Cole, B.B., Smith, R.W., Jenkins, K.M., Graham, B.B., Reynolds, P.R., and Reynolds, S.D. (2010). Tracheal Basal cells: a facultative progenitor cell pool. Am. J. Pathol. *177*, 362–376.

Dave, P.H., and Kwong, R.W.M. (2020). Cadmium exposure reduces the density of a specific ionocyte subtype in developing zebrafish. Chemosphere *244*, 125535.

Dobin, A., Davis, C.A., Schlesinger, F., Drenkow, J., Zaleski, C., Jha, S., Batut, P., Chaisson, M., and Gingeras, T.R. (2013). STAR: ultrafast universal RNA-seq aligner. Bioinformatics *29*, 15–21.

Domzalska, M., Zdrojewski, Z., Buda, N., Masiak, A., Szade, J., and Romanowicz, G. (2016). Symptoms mimicking Sjogren syndrome in a heterozygous carrier of CFTR deltaF508 mutation. Pol. Arch. Med. Wewn *126*, 895–896.

Durban, E.M., Barreto, P.D., Hilgers, J., and Sonnenberg, A. (1994). Cell phenotypes and differentiative transitions in mouse submandibular salivary gland defined with monoclonal antibodies to mammary epithelial cells. J. Histochem. Cytochem. *42*, 185–196.

Edlund, R.K., Birol, O., and Groves, A.K. (2015). The role of foxi family transcription factors in the development of the ear and jaw. Curr. Top. Dev. Biol. *111*, 461–495.

El Agha, E., Al Alam, D., Carraro, G., MacKenzie, B., Goth, K., De Langhe, S.P., Voswinckel, R., Hajihosseini, M.K., Rehan, V.K., and Bellusci, S. (2012). Characterization of a novel fibroblast growth factor 10 (Fgf10) knock-in mouse line to target mesenchymal progenitors during embryonic development. PLoS One *7*, e38452.

Entesarian, M., Dahlqvist, J., Shashi, V., Stanley, C.S., Falahat, B., Reardon, W., and Dahl, N. (2007). FGF10 missense mutations in aplasia of lacrimal and salivary glands (ALSG). Eur. J. Hum. Genet. *15*, 379–382.

Giffen, K.P., Liu, H., Kramer, K.L., and He, D.Z. (2019). Expression of protein-coding gene orthologs in zebrafish and mouse inner ear non-sensory supporting cells. Front Neurosci. *13*, 1117.

Graeff, R.W., Wang, G., and McCray, P.B., Jr. (1999). KGF and FGF-10 stimulate liquid secretion in human fetal lung. Pediatr. Res. *46*, 523–529.

Gromova, A., Voronov, D.A., Yoshida, M., Thotakura, S., Meech, R., Dartt, D.A., and Makarenkova, H.P. (2017). Lacrimal gland repair using progenitor cells. Stem Cells Transl. Med. *6*, 88–98.

Gu, Z., Gu, L., Eils, R., Schlesner, M., and Brors, B. (2014). Circlize Implements and enhances circular visualization in R. Bioinformatics *30*, 2811–2812.

Haan, N., Goodman, T., Najdi-Samiei, A., Stratford, C.M., Rice, R., El Agha, E., Bellusci, S., and Hajihosseini, M.K. (2013). Fgf10-expressing tanycytes add new neurons to the appetite/energy-balance regulating centers of the postnatal and adult hypothalamus. J. Neurosci. *33*, 6170–6180.

Hajihosseini, M.K., De Langhe, S., Lana-Elola, E., Morrison, H., Sparshott, N., Kelly, R., Sharpe, J., Rice, D., and Bellusci, S. (2008). Localization and fate of Fgf10-expressing cells in the adult mouse brain implicate Fgf10 in control of neurogenesis. Mol. Cell Neurosci. *37*, 857–868.

Hauser, B.R., Aure, M.H., Kelly, M.C., Genomics, Computational Biology, C., Hoffman, M.P., and Chibly, A.M. (2020). Generation of a single-cell RNAseq atlas of murine salivary gland development. iScience *23*, 101838.

Holliday, L.S. (2012). Editorial: vacuolar H(+)-ATPase: targeting a "housekeeping" enzyme for drug development. Curr. Protein Pept. Sci. *13*, 105–106.

Horng, J.L., Yu, L.L., Liu, S.T., Chen, P.Y., and Lin, L.Y. (2017). Potassium regulation in medaka (Oryzias latipes) larvae acclimated to fresh water: passive uptake and active secretion by the skin cells. Sci. Rep. *7*, 16215.

Hsu, H.H., Lin, L.Y., Tseng, Y.C., Horng, J.L., and Hwang, P.P. (2014). A new model for fish ion regulation: identification of ionocytes in freshwater- and seawater-acclimated medaka (Oryzias latipes). Cell Tissue Res. *357*, 225–243.

Izvolsky, K.I., Shoykhet, D., Yang, Y., Yu, Q., Nugent, M.A., and Cardoso, W.V. (2003). Heparan sulfate-FGF10 interactions during lung morphogenesis. Dev. Biol. *258*, 185–200.

Jacky, B.P., Garay, P.E., Dupuy, J., Nelson, J.B., Cai, B., Molina, Y., Wang, J., Steward, L.E., Broide, R.S., Francis, J., et al. (2013). Identification of fibroblast growth factor receptor 3 (FGFR3) as a protein receptor for botulinum neurotoxin serotype A (BoNT/A). PLoS Pathog. *9*, e1003369.

Jalali, R., Lodder, J.C., Zandieh-Doulabi, B., Micha, D., Melvin, J.E., Catalan, M.A., Mansvelder, H.D., DenBesten, P., and Bronckers, A. (2017). The role of Na:K:2Cl cotransporter 1 (NKCC1/SLC12A2) in dental epithelium during enamel formation in mice. Front Physiol. *8*, 924.

Jaskoll, T., Abichaker, G., Witcher, D., Sala, F.G., Bellusci, S., Hajihosseini, M.K., and Melnick, M. (2005). FGF10/FGFR2b signaling plays essential roles during *in vivo* embryonic submandibular salivary gland morphogenesis. BMC Dev. Biol. *5*, 11.

Jaskoll, T., Zhou, Y.M., Chai, Y., Makarenkova, H.P., Collinson, J.M., West, J.D., Hajihosseini, M.K., Lee, J., and Melnick, M. (2002). Embryonic submandibular gland morphogenesis: stage-specific protein localization of FGFs, BMPs, Pax6 and Pax9 in normal mice and abnormal SMG phenotypes in FgfR2-IIIc(+/Delta), BMP7(-/-) and Pax6(-/-) mice. Cells Tissues Organs *170*, 83–98.

Jirakulsomchok, D., and Schneyer, C.A. (1979). alpha- and beta-Adrenergic effects on Na, K, Cl, and HCO_3 transport in perfused salivary duct during sympathetic nerve stimulation. Proc. Soc. Exp. Biol. Med. *161*, 479–483.

Kalajzic, Z., Li, H., Wang, L.P., Jiang, X., Lamothe, K., Adams, D.J., Aguila, H.L., Rowe, D.W., and Kalajzic, I. (2008). Use of an alpha-smooth muscle actin GFP reporter to identify an osteoprogenitor population. Bone *43*, 501–510.

Kelly, R.G., Brown, N.A., and Buckingham, M.E. (2001). The arterial pole of the mouse heart forms from Fgf10-expressing cells in pharyngeal mesoderm. Dev. Cell *1*, 435–440.

Kurabuchi, S. (2006). Repeated androgen and thyroid hormone injection modulates the morphology of hormone-responsive duct cells in the mouse parotid gland. Odontology *94*, 29–37.

Kurabuchi, S., Yao, C., Chen, G., and Hosoi, K. (2019). Reversible conversion among subtypes of salivary gland duct cells as identified by production of a variety of bioactive polypeptides. Acta Histochem. Cytochem. *52*, 59–65.

Kwak, M., Ninche, N., Klein, S., Saur, D., and Ghazizadeh, S. (2018). c-Kit(+) cells in adult salivary glands do not function as tissue stem cells. Sci. Rep. *8*, 14193.

Leach, J.P., and Morrisey, E.E. (2018). Repairing the lungs one breath at a time: how dedicated or facultative are you? Genes Dev. *32*, 1461–1471.

Lee, D.H., Oh, I.Y., Koo, K.T., Suk, J.M., Jung, S.W., Park, J.O., Kim, B.J., and Choi, Y.M. (2015). Improvement in skin wrinkles using a preparation containing human growth factors and hyaluronic acid serum. J. Cosmet. Laser Ther. *17*, 20–23.

Lee, M.G., Ohana, E., Park, H.W., Yang, D., and Muallem, S. (2012). Molecular mechanism of pancreatic and salivary gland fluid and HCO_3 secretion. Physiol. Rev. *92*, 39–74.

Lorin-Nebel, C., Boulo, V., Bodinier, C., and Charmantier, G. (2006). The $Na^+/K^+/2Cl^-$ cotransporter in the sea bass Dicentrarchus labrax during ontogeny: involvement in osmoregulation. J. Exp. Biol. *209*, 4908–4922.

Love, M.I., Huber, W., and Anders, S. (2014). Moderated estimation of fold change and dispersion for RNA-seq data with DESeq2. Genome Biol. *15*, 550.

Luo, X., Choi, J.Y., Ko, S.B., Pushkin, A., Kurtz, I., Ahn, W., Lee, M.G., and Muallem, S. (2001). HCO3- salvage mechanisms in the submandibular gland acinar and duct cells. J. Biol. Chem. *276*, 9808–9816.

Makarenkova, H.P., Hoffman, M.P., Beenken, A., Eliseenkova, A.V., Meech, R., Tsau, C., Patel, V.N., Lang, R.A., and Mohammadi, M. (2009). Differential interactions of FGFs with heparan sulfate control gradient formation and branching morphogenesis. Sci. Signal *2*, ra55.

Martin, K.E., Ehrman, J.M., Wilson, J.M., Wright, P.A., and Currie, S. (2019). Skin ionocyte remodeling in the amphibious mangrove rivulus fish (Kryptolebias marmoratus). J. Exp. Zool A. Ecol. Integr. Physiol. *331*, 128–138.

Martin, M. (2011). Cutadapt removes adapter sequences from high-throughput sequencing reads. EMBnet *17*, 10–12.

Masuhara, M., Nagao, K., Nishikawa, M., Sasaki, M., Yoshimura, A., and Osawa, M. (2000). Molecular cloning of murine STAP-1, the stem-cell-specific adaptor protein containing PH and SH2 domains. Biochem. biophysical Res. Commun. *268*, 697–703.

Meyerholz, D.K., Stoltz, D.A., Gansemer, N.D., Ernst, S.E., Cook, D.P., Strub, M.D., LeClair, E.N., Barker, C.K., Adam, R.J., Leidinger, M.R., et al. (2018). Lack of cystic fibrosis transmembrane conductance regulator disrupts fetal airway development in pigs. Lab Invest. *98*, 825–838.

Mikolajczak, M., Goodman, T., and Hajihosseini, M.K. (2016). Interrogation of a lacrimo-auriculo-dento-digital syndrome protein reveals novel modes of fibroblast growth factor 10 (FGF10) function. Biochem. J. *473*, 4593–4607.

Milunsky, J.M., Zhao, G., Maher, T.A., Colby, R., and Everman, D.B. (2006). LADD syndrome is caused by FGF10 mutations. Clin. Genet. *69*, 349–354.

Montoro, D.T. (2019). Rare Cells Play Central Roles in Airway Maintenance. Doctoral dissertation (Harvard University, Graduate School of Arts & Sciences), 0000-0002-6222-2149.

Montoro, D.T., Haber, A.L., Biton, M., Vinarsky, V., Lin, B., Birket, S.E., Yuan, F., Chen, S., Leung, H.M., Villoria, J., et al. (2018). A revised airway epithelial hierarchy includes CFTR-expressing ionocytes. Nature *560*, 319–324.

Mori, M., Namba, M., Muramatsu, Y., Sumitomo, S., Takai, Y., and Shikimori, M. (2011). Endothelin expression in salivary gland. Int. J. Oral Sci. *8*, 7–10.

Morrell, J.I., Gresik, E.W., and Barka, T. (1987). Autoradiographic localization of dihydrotestosterone binding in the major salivary glands and other androgen-responsive organs of the mouse. J. Histochem. Cytochem. *35*, 1053–1058.

Mukherjee, M., deRiso, J., Otterpohl, K., Ratnayake, I., Kota, D., Ahrenkiel, P., Chandrasekar, I., and Surendran, K. (2019). Endogenous notch signaling in adult kidneys maintains segment-specific epithelial cell types of the distal tubules and collecting ducts to ensure water homeostasis. J. Am. Soc. Nephrol. *30*, 110–126.

Noel, S., Strale, P.O., Dannhoffer, L., Wilke, M., DeJonge, H., Rogier, C., Mettey, Y., and Becq, F. (2008). Stimulation of salivary secretion *in vivo* by CFTR potentiators in Cftr+/+ and Cftr-/- mice. J. Cyst Fibros *7*, 128–133.

Ono Minagi, H., Sarper, S.E., Kurosaka, H., Kuremoto, K.I., Taniuchi, I., Sakai, T., and Yamashiro, T. (2017). Runx1 mediates the development of the granular convoluted tubules in the submandibular glands. PLoS One *12*, e0184395.

Paranjape, S.M., and Zeitlin, P.L. (2008). Atypical cystic fibrosis and CFTR-related diseases. Clin. Rev. Allergy Immunol. *35*, 116–123.

Pardini, L.C., and Taga, R. (1996). Stereological study of the sexual dimorphism in mouse submandibular glands. Okajimas Folia Anat. Jpn. *73*, 119–124.

Petiot, A., Conti, F.J., Grose, R., Revest, J.M., Hodivala-Dilke, K.M., and Dickson, C. (2003). A crucial role for Fgfr2-IIIb signalling in epidermal development and hair follicle patterning. Development *130*, 5493–5501.

Pirani, D., Evans, L.A., Cook, D.I., and Young, J.A. (1987). Intracellular pH in the rat mandibular salivary gland: the role of Na-H and Cl-HCO_3 antiports in secretion. Pflugers Arch. *408*, 178–184.

Plasschaert, L.W., Zilionis, R., Choo-Wing, R., Savova, V., Knehr, J., Roma, G., Klein, A.M., and Jaffe, A.B. (2018). A single-cell atlas of the airway epithelium reveals the CFTR-rich pulmonary ionocyte. Nature *560*, 377–381.

Prince, L.S. (2018). FGF10 and human lung disease across the Life spectrum. Front Genet. *9*, 517.

Quigley, I.K., Stubbs, J.L., and Kintner, C. (2011). Specification of ion transport cells in the Xenopus larval skin. Development *138*, 705–714.

Ramilowski, J.A., Goldberg, T., Harshbarger, J., Kloppmann, E., Lizio, M., Satagopam, V.P., Itoh, M., Kawaji, H., Carninci, P., Rost, B., et al. (2015). A draft network of ligand-receptor-mediated multicellular signalling in human. Nat. Commun. *6*, 7866.

Ramilowski, J.A., Goldberg, T., Harshbarger, J., Kloppmann, E., Lizio, M., Satagopam, V.P., Itoh, M., Kawaji, H., Carninci, P., Rost, B., et al. (2016). Corrigendum: a draft network of ligand-receptor-mediated multicellular signalling in human. Nat. Commun. *7*, 10706.

Rocchi, C., Barazzuol, L., and Coppes, R.P. (2021). The evolving definition of salivary gland stem cells. NPJ Regen. Med. *6*, 4.

Roussa, E., Thevenod, F., Sabolic, I., Herak-Kramberger, C.M., Nastainczyk, W., Bock, R., and Schulz, I. (1998). Immunolocalization of vacuolar-type H+-ATPase in rat submandibular gland and adaptive changes induced by acid-base disturbances. J. Histochem. Cytochem. *46*, 91–100.

Rugel-Stahl, A., Elliott, M.E., and Ovitt, C.E. (2012). Ascl3 marks adult progenitor cells of the mouse salivary gland. Stem Cell Res. *8*, 379–387.

Sahara, Y., Horie, S., Fukami, H., Goto-Matsumoto, N., and Nakanishi-Matsui, M. (2015). Functional roles of V-ATPase in the salivary gland. J. Oral Biosciences *57*, 102–109.

Sato, A., Hamano, M., and Miyoshi, S. (1998). Increasing frequency of occurrence of tuft cells in the main excretory duct during postnatal development of the rat submandibular gland. Anat. Rec. *252*, 276–280.

Sato, A., and Miyoshi, S. (1988). Ultrastructure of the main excretory duct epithelia of the rat parotid and submandibular glands with a review of the literature. Anat. Rec. *220*, 239–251.

Sato, A., and Miyoshi, S. (1997). Fine structure of tuft cells of the main excretory duct epithelium in the rat submandibular gland. Anat. Rec. *248*, 325–331.

Shams, I., Rohmann, E., Eswarakumar, V.P., Lew, E.D., Yuzawa, S., Wollnik, B., Schlessinger, J., and Lax, I. (2007). Lacrimo-auriculo-dento-digital syndrome is caused by reduced activity of the fibroblast growth factor 10 (FGF10)-FGF receptor 2 signaling pathway. Mol. Cell. Biol. *27*, 6903–6912.

Shaughnessy, C.A., and McCormick, S.D. (2020). Functional characterization and osmoregulatory role of the Na(+)-K(+)-2Cl(-) cotransporter in the gill of sea lamprey (Petromyzon marinus), a basal vertebrate. Am. J. Physiol. Regul. Integr. Comp. Physiol. *318*, R17–R29.

Shin, Y.H., Lee, S.W., Kim, M., Choi, S.Y., Cong, X., Yu, G.Y., and Park, K. (2016). Epigenetic regulation of CFTR in salivary gland. Biochem. Biophys. Res. Commun. *481*, 31–37.

Shono, T., Kurokawa, D., Miyake, T., and Okabe, M. (2011). Acquisition of glial cells missing 2 enhancers contributes to a diversity of ionocytes in zebrafish. PLoS One *6*, e23746.

Short, D.B., Trotter, K.W., Reczek, D., Kreda, S.M., Bretscher, A., Boucher, R.C., Stutts, M.J., and Milgram, S.L. (1998). An apical PDZ protein anchors the cystic fibrosis transmembrane conductance regulator to the cytoskeleton. J. Biol. Chem. *273*, 19797–19801.

Shubin, A.D., Sharipol, A., Felong, T.J., Weng, P.L., Schutrum, B.E., Joe, D.S., Aure, M.H., Benoit, D.S.W., and Ovitt, C.E. (2020). Stress or injury induces cellular plasticity in salivary gland acinar cells. Cell Tissue Res. *380*, 487–497.

Stuart, T., Butler, A., Hoffman, P., Hafemeister, C., Papalexi, E., Mauck, W.M., 3rd, Hao, Y., Stoeckius, M., Smibert, P., and Satija, R. (2019). Comprehensive integration of single-cell data. Cell *177*, 1888–1902.e1821.

Sun, D.I., Tasca, A., Haas, M., Baltazar, G., Harland, R.M., Finkbeiner, W.E., and Walentek, P. (2018). Na^+/H^+ exchangers are required for the development and function of vertebrate mucociliary epithelia. Cells Tissues Organs *205*, 279–292.

Takei, Y., Hiroi, J., Takahashi, H., and Sakamoto, T. (2014). Diverse mechanisms for body fluid regulation in teleost fishes. Am. J. Physiol. Regul. Integr. Comp. Physiol. *307*, R778–R792.

Takeyama, A., Yoshikawa, Y., Ikeo, T., Morita, S., and Hieda, Y. (2015). Expression patterns of CD66a and CD117 in the mouse submandibular gland. Acta Histochem. *117*, 76–82.

Thotakura, S., Basova, L., and Makarenkova, H.P. (2019). FGF gradient controls boundary position between proliferating and differentiating cells and regulates lacrimal gland growth dynamics. Front Genet. *10*, 362.

Thulesen, J., Bor, M.V., Thulesen, S., Nexo, E., Poulsen, S.S., and Jorgensen, P.E. (2002). Altered secretion and processing of epidermal growth factor in adrenergic-induced growth of the rat submandibular gland. Regul. Pept. *106*, 105–114.

Trayer, V., Sejourne, N., Gay, S., and Thermes, V. (2015). Evidence for two distinct waves of epidermal ionocyte differentiation during medaka embryonic development. Dev. Dyn. *244*, 888–902.

Vieira Braga, F.A., Kar, G., Berg, M., Carpaij, O.A., Polanski, K., Simon, L.M., Brouwer, S., Gomes, T., Hesse, L., Jiang, J., et al. (2019). A cellular census of human lungs identifies novel cell states in health and in asthma. Nat. Med. *25*, 1153–1163.

Wang, G., Lou, H.H., Salit, J., Leopold, P.L., Driscoll, S., Schymeinsky, J., Quast, K., Visvanathan, S., Fine, J.S., Thomas, M.J., et al. (2019). Characterization of an immortalized human small airway basal stem/progenitor cell line with airway region-specific differentiation capacity. Respir. Res. *20*, 196.

Wang, L., Wang, S., and Li, W. (2012). RSeQC: quality control of RNA-seq experiments. Bioinformatics *28*, 2184–2185.

Yamamoto-Hino, M., Miyawaki, A., Segawa, A., Adachi, E., Yamashina, S., Fujimoto, T., Sugiyama, T., Furuichi, T., Hasegawa, M., and Mikoshiba, K. (1998). Apical vesicles bearing inositol 1,4,5-trisphosphate receptors in the Ca^{2+} initiation site of ductal epithelium of submandibular gland. J. Cell Biol *141*, 135–142.

Yang, N.Y., Mukaibo, T., Gao, X., Kurtz, I., and Melvin, J.E. (2019). Slc4a11 disruption causes duct cell loss and impairs NaCl reabsorption in female mouse submandibular glands. Physiol. Rep. *7*, e14232.

Yokoyama, T., Takemoto, M., Hirakawa, M., and Saino, T. (2019). Different immunohistochemical localization for TMEM16A and CFTR in acinar and ductal cells of rat major salivary glands and exocrine pancreas. Acta Histochem. *121*, 50–55.

Zeng, M., Szymczak, M., Ahuja, M., Zheng, C., Yin, H., Swaim, W., Chiorini, J.A., Bridges, R.J., and Muallem, S. (2017). Restoration of CFTR activity in ducts rescues acinar cell function and reduces inflammation in pancreatic and salivary glands of mice. Gastroenterology *153*, 1148–1159.

Zhang, W., Ogando, D.G., Kim, E.T., Choi, M.J., Li, H., Tenessen, J.M., and Bonanno, J.A. (2017). Conditionally immortal Slc4a11-/- mouse corneal endothelial cell line recapitulates disrupted glutaminolysis seen in Slc4a11-/- mouse model. Invest. Ophthalmol. Vis. Sci. *58*, 3723–3731.

Zheng, W., Ma, M., Du, E., Zhang, Z., Jiang, K., Gu, Q., and Ke, B. (2015). Therapeutic efficacy of fibroblast growth factor 10 in a rabbit model of dry eye. Mol. Med. Rep. *12*, 7344–7350.

Zinkle, A., and Mohammadi, M. (2019). Structural biology of the FGF7 subfamily. Front Genet. *10*, 102.

Zinn, V.Z., Khatri, A., Mednieks, M.I., and Hand, A.R. (2015). Localization of cystic fibrosis transmembrane conductance regulator signaling complexes in human salivary gland striated duct cells. Eur. J. Oral Sci. *123*, 140–148.

Zyrianova, T., Basova, L.V., and Makarenkova, H. (2019). Isolation of myoepithelial cells from adult murine lacrimal and submandibular glands. J. Vis. Exp. https://doi.org/10.3791/59602.

STAR★METHODS

KEY RESOURCES TABLE

REAGENT or RESOURCE	SOURCE	IDENTIFIER
Antibodies		
Monoclonal Anti-Actin, α-Smooth Muscle (α-SMA) (1A4), Mouse IgG2a (1:400)	Sigma	A2547; RRID:AB_476701
Recombinant Aquaporin-5 monoclonal antibody (EPR3747), rabbit (1:1000)	Abcam	ab92320; RRID:AB_2049171
Polyclonal Goat anti-Mouse ASCL3, goat (1:100)	LSBio	LS-B8350-50; RRID:AB_900923
CFTR Monoclonal Antibody (M3A7), mouse IgG1 (1:100-1:200)	Invitrogen	MA5-11768; RRID:AB_10983660
Claudin 1 Monoclonal Antibody (2H10D10), mouse IgG1 (1:100)	Thermo Fisher Scientific	37-4900; RRID:AB_2533323
Rabbit anti-dtTomato/dsRed (1:1000)	Clontech	632496; RRID:AB_10013483
Rabbit anti-EGF (1:200)	Gift from Edward W. Gresik	N/A
Mouse E-Cadherin purified monoclonal antibody (36/E-Cadherin), mouse IgG2a, κ (1:200)	BD Biosciences	610182; RRID:AB_397581
Rat CD326 (EpCAM)-APC monoclonal antibody (G8.8), rat IgG2a, kappa	eBioscience	17-579182; RRID:AB_2716944
Recombinant FGFR2 monoclonal antibody N-terminal (SP273), rabbit (1:400)	Abcam	ab227683
Rabbit polyclonal Foxi1 antibody (1:100)	Sigma	SAB4500922; RRID:AB_10761468
Rabbit Cytokeratin 7 monoclonal antibody (RCK105), rabbit (1:200)	Abcam	ab9021; RRID:AB_306947
Goat polyclonal NKCC1 Antibody (N-16), goat (1:100)	Santa Cruz Biotechnology	sc-21545; RRID:AB_2188633
Recombinant rabbit Panx1 polyclonal antibody (1:100)	Millipore/Sigma	HPA016930; RRID:AB_1854954
Mouse Vimentin monoclonal antibody (3H9D1), mouse IgG1 (1:100)	Proteintech	60330-1-Ig; RRID:AB_2881439
Rat monoclonal (pSer28) phosphorylated histone H3 antibody (1:100)	Sigma-Aldrich	H9908; RRID:AB_260096
Goat anti-Mouse IgG (H+L), Alexa Fluor (1:200)	ThermoFisher Scientific	N/A
Goat anti-Mouse IgG1, Alexa Fluor (1:200)	ThermoFisher Scientific	N/A
Goat anti-Mouse IgG2a, Alexa Fluor (1:200)	ThermoFisher Scientific	N/A
Goat anti-Rabbit IgG (H+L), Alexa Fluor (1:200)	ThermoFisher Scientific	N/A
Chicken anti-Goat IgG (H+L) Cross-Adsorbed Secondary Antibody, Alexa Fluor (1:200)	ThermoFisher Scientific	N/A
Goat Anti-Rabbit IgG Antibody (H+L), Biotinylated (1:200)	Vector Labs	BA-1000-1.5; RRID:AB_2313606
Phycoerythrin (PE) rat anti-mouse Ly-6A/E (Sca1), (E13-161.7)	BD Biosciences	553336; RRID:AB_394792
PE-Cy7 rat anti-mouse CD31	BD Biosciences	561410; RRID:AB_10612003
FITC rat anti-mouse CD34	BD Biosciences	553733; RRID:AB_395017
Allophycocyanin (APC)-eFluor 780 anti-mouse CD117 (c-Kit)	eBioscience	47-1171-80; RRID:AB_1272213

(*Continued on next page*)

Continued

REAGENT or RESOURCE	SOURCE	IDENTIFIER
APC anti-mouse CD326 (EpCAM) (G8.8)	eBioscience	17-5791-80; RRID:AB_2734965
12 nm Colloidal Gold AffiniPure Goat Anti-Rabbit IgG (H+L) (EM Grade) (1:200)	Jackson Immuno-Research	111-205-144; RRID:AB_2338016
DAPI	Bio-Techne/Tocris	5748
Chemicals, peptides, and recombinant proteins		
2-Methylbutane	Sigma	320404-1L
70% ethanol	Fisher Scientific	BP8201-500
Ethyl alcohol, Pure (100%)	Millipore/Sigma	E7023-500ML
Accutase	Sigma	A6964
Antibiotic-Antimycotic	Gibco	15240-062
biotin/avidin-peroxidase	Sigma	A6003
CaCl2 (1 M solution)	BioVision	B1010-100
Collagenase I	Worthington	LS004194
Collagenase IV	Sigma	C5138
Dispase II	Sigma	D4693
DMEM low glucose	Sigma	D5546
DNase I	Akron Biotech	AK37778–0050
Dulbecco's Modified Eagle's Medium/F12 (DMEM/F12)	Millipore	DF-042-B
High glucose DMEM	Thermo Fisher Scientific	11995073
Ethanol	MilliporeSigma	EX0276-6
Ethylenediaminetetraacetic acid (EDTA, 0.5 M solution)	Gibco (Thermo Fisher Scientific)	15575-038
Fisherbrand™ Cover Glasses: Rectangles	Fisher Scientific	12-545-M
Fluorescence Mounting Medium	DAKO	S302380
Fluoromount-G	SouthernBiotech	0100-01
Frozen Tissue Slide Pack	Fisher Scientific	15-188-48
FxCycle Violet stain	ThermoFisher Scientific	F10347
Gill Hematoxylin Stain	Fisher Scientific	CS400-1D
Glutamax	Gibco	35050-061
Glutaraldehyde	Sigma	G-5882
Hank's Balanced Salt Solution (HBSS)	Corning (Thermo Fisher Scientific)	21-022-CV
HEPES (1 M solution)	Sigma	H0887
Methanol (Certified ACS)	Fisher Scientific	A412
Nova Red	Vector Labs	SK-4800; RRID:AB_2336845
Paraformaldehyde, granular, EM Grade, purified	VWR	100504-160
Glutaraldehyde, 25% Aqueous Solution	Millipore/Sigma	354400
Sodium cacodylate trihydrate	Millipore/Sigma	C0250-25G
LR White Embedding Medium	Electron Microscopy Sciences	14381
Grids for Electron Microscopy (200 mesh nickel grids)	Electron Microscopy Sciences	EMS200-Cu, Cu-Rh, Ni
Uranyl acetate	Electron Microscopy Sciences	22400
Tween 20	Fisher Scientific	MP1TWEEN201
Donor Goat Serum	Fisher Scientific	NBO36768
Phosphate Buffered Saline (PBS) tablets	Sigma	P4417
Poly-L-lysiine solution	Sigma	P8920-500ML
Qiazol lysis reagent	Qiagen	79306
Tamoxifen	Sigma	T5648-1G

(*Continued on next page*)

Continued		
REAGENT or RESOURCE	SOURCE	IDENTIFIER
Tissue-Plus™ O.C.T. Compound	Fisher Scientific	23-730-571
Tris-buffered saline	Boston Bioproduct	BM-301B
Critical commercial assays		
miRNeasy Micro Kit	Qiagen	217084
SMART-Seq HT	Takara	634456
Corning Matrigel Growth Factor Reduced (GFR) Basement Membrane Matrix	Millipore/Sigma	CLS354230-1EA
Deposited data		
Bulk RNAseq data	This study	GEO: GSE188904
scRNA-seq data, mouse SMG	(Hauser et al., 2020)	GEO: GSE150327
The Human Protein Atlas	https://www.proteinatlas.org	N/A
scRNA-seq data, mouse pulmonary cells	(Plasschaert et al., 2018)	GEO: GSE102580
Experimental models: Organisms/strains		
Fgf10^{CreERT2} mouse	(El Agha et al., 2012; Haan et al., 2013)	N/A
ROSA26-Tomato mouse (B6.Cg-Gt(ROSA) 26Sor$^{tm9(CAG-tdTomato)Hze}$/J)	The Jackson Laboratory	Strain:#007909; RRID:IMSR_JAX:007909
Fgf10^{LacZ} mouse	(Kelly et al., 2001)	N/A
αSMA-GFP mouse	(Kalajzic et al., 2008)	N/A
ICR mouse	Envigo	ICR (CD-1®)
Oligonucleotides		
RNA probe for *Foxi1*	ACDBio	N/A
RNA probe for *Ascl3*	ACDBio	N/A
RNA probe for *Fgf10*	ACDBio	N/A
Software and algorithms		
Excel	Microsoft	N/A
FACSDiva	BD Bioscience	N/A
FlowJo	FlowJo, LLC	N/A
ImageJ	NIH	N/A
IMARIS	Oxford Instruments	N/A
Prism 9 v9.1.2	GraphPad	N/A
RStudio 1.4.1717	RStudio, Inc.	N/A
R version 4.1.2	R Foundation for Statistical Computing	https://www.r-project.org/
Seurat v 4.05	(Stuart et al., 2019)	https://github.com/satijalab/seurat
Word	Microsoft	N/A

RESOURCE AVAILABILITY

Lead contact

Further information and requests for resources and reagents should be directed to and will be fulfilled by the lead contact - Helen P. Makarenkova (hmakarenk@scripps.edu).

Materials availability

This study did not generate new unique reagents.

Data and code availability

- The RNAseq data of FACS sorted FGF10 expressing cells have been deposited at Gene Expression Omnibus (GEO) under the accession number GEO: GSE188904.
- The single-cell RNA sequencing dataset is previously published and publicly available (GEO: GSE150327). Ready-to-use SEURAT object are also available via figshare (Postnatal SMG integrated dataset: Figshare: https://doi.org/10.6084/m9.figshare.13157726).

- All original code is available in paper's supplemental information.
- Any additional information required to reanalyze data from this study is available from the lead contact upon request.

EXPERIMENTAL MODEL

Mice

All experiments were carried out in accordance with the ARVO statement for the Use of Animals in Ophthalmic and Vision Research and were approved by the Scripps Research Institute and the Gavin Herbert Eye Institute Animal Care and Use Committees.

Fgf10^{CreERT2}*:Rosa26*^{Tomato} mice were generated by crossing *Fgf10*^{CreERT2} (Haan et al., 2013) mice with *ROSA26-Tomato* reporter strains (The Jackson Laboratory stock and #007909, also referred as Ai9 mice).Both males and females were used between P1 and P350 in all experiments. Fgf10LacZ mice were described previously (Kelly et al., 2001) and analyzed at 2 M of age. To isolate myoepithelial cells (MECs) we used the α-smooth muscle actin-GFP 2 M old male mice (αSMA-GFP) (Kalajzic et al., 2008). All strains were maintained on a C57BL/6J background. For *in situ* hybridization, ICR mice (CD-1®) were purchased from Envigo and cared for and maintained at the NIDCR Veterinary Resource Core in accordance with institutional and IACUC guidelines. Mice of both sexes at P1 - P60 were used for experiments. All mice were fed ad libitum and kept under 12-h light/12-h dark cycle.

METHOD DETAILS

Tamoxifen preparation and administration

Tamoxifen (TM, 1 g) (Sigma, #T5648-1G) was dissociated in 2 mL ethanol and diluted in filtered corn oil. The solution was vortexed and placed on shaker at 45°C overnight. When completely dissolved, aliquots (20 mg/mL of TM) were stored at −80°C. TM was administered by intraperitoneal injection (0.1 mg per g of weight) at indicated times.

Immunohistochemistry on paraffin sections

Tissues were fixed immediately and embedded in paraffin in Scripps histology core facility, and 5 μm sections were prepared. Endogenous peroxidase activity on rehydrated sections was blocked by treating slides with 3% hydrogen peroxide in absolute methanol for 30 min. Antigen retrieval was performed for 40 min using 0.01 M citrate (pH 6.0) in a humidified heated chamber. Sections were blocked with 5 g/L casein in PBS containing 0.5 g/L thimerosal (Sigma-Aldrich; cat# T5125-25G) for 30 min, and incubated with anti-DsRed primary antibody, and diluted in casein buffer overnight at 4°Cand anti-dsRed primary antibodies were used for immunostaining. Biotinylated secondary antibodies (Vector Labs, Burlingame, CA) were used at a 1:300 dilution. Visualization was achieved using biotin/avidin-peroxidase (Vector Labs) and Nova Red (Vector Labs). Tissue was counterstained with Gill's hematoxylin (Fisher Scientific, San Diego, CA; CS400).

Immunoelectron microscopy

Mice were initially perfused with 4% paraformaldehyde and SMGs were dissected divided into lobules and post-fixed in 2.5% glutaraldehyde (Millipore/Sigma, #354400) in 0.1 M cacodylate buffer for 2 h, tissue was washed in 0.1 M cacodylate buffer (Millipore/Sigma, #C0250-25G) and dehydrated through a graded series of ethanol (50%, 70%, 90%, 100%, 100%), infiltrated with a 1:1 mixture of 100% ethanol (Millipore/Sigma, #E7023-500ML) and LR White for 1 h, and then infiltrated with LR White resin (Electron Microscopy sciences, #14381) at 4°C overnight. The following day, the tissues were infiltrated with fresh LR White and embedded. Silver-grey sections were cut with a Reinhart ultramicrotome and collected on 200 mesh nickel grids (Electron Microscopy sciences, #EMS200-Cu, Cu-Rh, Ni).

Sections were first blocked with 4% BSA + 2% whole goat serum (Fisher Scientific, # NBO36768) + 0.1% Tween 20 (Fisher Scientific, #MP1TWEEN201) in PBS for 30 min. After blocking, sections were incubated on drops of the primary antibody (polyclonal anti-DsRed, Clontech Ab # 632496), diluted 1:200 in 2% BSA + 1% whole goat serum + 0.1% Tween 20 in PBS overnight at 4°C. Following incubation in primary antibody, the sections were washed twice (5 min each) in PBS. The sections were then incubated in secondary antibody (12 nm gold-conjugated goat anti-rabbit IgG (H+L), Jackson ImmunoResearch, # 111-205-144) diluted 1:20 in PBS at room temperature for 2 h. Sections were then washed with PBS and post-fixed with 2% glutaraldehyde in water for 5 min. Following post-fixation, the sections were washed twice (2 min each) with water, stained with uranyl acetate (Electron Microscopy Sciences, #22400) for 2 min and then washed briefly with water.

Images were collected on a Philips CM100 transmission electron microscope equipped with a Soft Imaging Systems MegaView III CCD camera.

Frozen sections preparation and immunostaining

SGs dissected from mice were fixed with 2% PFA in PBS (pH 7.4) for 1 h and processed for whole-mount immunostaining (see below) or frozen in 2-methylbutane (isopentane; Sigma-Aldrich, St. Louis, MO, USA) cooled by liquid nitrogen, and 15 μm sections were cut with a Hacker/Bright OTF5000-LS004 Cryostat (Hacker Industries Inc., UK). Sections were blocked with 5% BSA in Tris-buffered saline containing 0.05% Tween 20 (TBST) and then incubated with appropriate primary antibodies at 4°C overnight. The following

antibodies were used mouse monoclonal to α-SMA (clone 1A4,# A2547, Sigma-Aldrich), rabbit monoclonal to Aquaporin 5 (clone EPR3747, #ab92320, Abcam), mouse monoclonal to CFTR (clone M3A7, #MA5-11768, Invitrogen), mouse monoclonal to Claudin 1 (#37-4900, Thermo Fisher Scientific), mouse monoclonal to E-Cadherin (#610182, BD Biosciences), rabbit polyclonal to Fgfr2 (#F0300, Sigma-Aldrich), rabbit polyclonal toFoxi1 (#SAB4500922, Sigma-Aldrich), mouse monoclonal to Cytokeratin-7 (#Ab9021, Abcam), goat polyclonal to Nkcc1 (#sc-21545, Santa Cruz Biotechnology), rabbit polyclonal to Panx1 (#HPA016930, Sigma-Aldrich), Vimentin (#60330-1-Ig, ProteinTech), β-Galactosidase antibody (#ab221199, Abcam), and goat polyclonal antibody to Ascl3 (#LS-B8350, LsBio). The EGF antibody was kind gift from Dr. Edward W. Gresik. Appropriate secondary antibodies were purchased from Thermo Fisher Scientific (Molecular Probes, Waltham, MA). Then, sections were washed three times and nuclei were counter-stained with DAPI for 20 min at RT. Slides were mounted with Fluoromount-G (#0100-01, SouthernBiotech, Birmingham, AL). Images were taken using a Zeiss LSM 880 laser scanning confocal microscope.

In situ hybridization

Dissection tools were cleaned with 70% ethanol and wiped before SMG isolation from P1 and adult ICR mice. The tissue was fixed 4%PFA for no longer than 36hrs. The samples were paraffine embedded and sections were cut by Histoserv Inc. *In situ* hybridization was performed by Advanced Cell Diagnostics with probes for *Ascl3, Foxi1* and *Fgf10*. Specific probe sequences are proprietary and generated with RNAscope® technology by Advanced Cell Diagnostics.

Cell isolation from SMGs and FACS sorting

All solutions were prepared in sterile conditions. First, SMGs were quickly minced in a dish filled with 2 mL of digestion medium (DMEM low glucose (SigmaD5546), Glutamax (Gibco 35050-061), Antibiotic-Antimycotic (Gibco 15240-062), 4.5 mg/mL collagenase I (Worthington LS004194), 2.4 U/mL dispase II (Sigma D4693), DNAse 50 U/mL (Akron Biotech, AK37778–0050), transferred to 2 mL-tubes and incubated for 90 min at 37°C and 80 rpm. Every 30 min, samples were gently triturated by pipetting up and down 20-30 times with a wide-bored pipet tip. Finally, cell clusters were broken by passing the sample 3 times through an insulin syringe needle (31G). Cell suspension was transferred to a 15 mL tube with blocking medium (DMEM/F-12 (Millipore DF-042-B), 15% FBS, Glutamax (Gibco 35050-061), Antibiotic-Antimycotic (Gibco 15240-062), 2 mM EDTA) was added to a total of 5 mL. Cell suspension was filtered two times through 70-μm cell strainers, washed with 1 mL of blocking media. Samples were centrifuged at 300 × g for 5 min at RT. Supernatant was discarded and 1 mL of accutase (Sigma, A6964) was added. After 3 min at 37°C, 100 rpm, accutase was inactivated by the addition of blocking medium. Cells were pelleted and incubated for 30 min at RT with HBSS supplemented with 10 mM HEPES, 5 mM $MgCl_2$ and 50 U/mL DNase I. Cells were resuspended in 100 μL of FACS buffer (DPBS, 2.5% FBS and 1 mM EDTA). For flow cytometry analysis, approximately 0.5×10^6 cells were pelleted at 400 × g for 10 min at 4°C and resuspended in 100 μL of staining buffer with the anti-mouse CD326 (EpCAM) APC conjugated (# 17-5791-82, eBioscience). A viability dye was added (FxCycle Violet stain, #F10347, Molecular probes by Life Technologies) to discriminate dead/live cells. For FACS analysis, approximately 0.5×10^6 cells were pelleted at 1,200 g for 10 min at 4°C and resuspended in 100 μL of staining buffer with the anti-mouse CD326 (EpCAM) APC conjugated (# 17-5791-82, eBioscience).

Cell sorting of $FGF10^{pos}$ cells was performed at the TSRI Flow Cytometry Core Facility by using MoFlo Astrios EQ jet-in-air sorting flow cytometer (Beckman Coulter). Cells were sorted at 25 psi through a 100 μm nozzle into a tube filled with FACS buffer. The main population of cells was determined by forward scatter (FSC) and side scatter (SSC) area gating, as well as dead cell exclusion. Doublets were excluded via FSC-Area vs Width and SSC-Area vs SSC-Width. Data analyses were performed by using FlowJo software.

RNA extraction

Sorted cells were pelleted and resuspended with 700 μL Qiazol lysis reagent (#79306, Qiagen). RNA was isolated with the miRNeasy Micro Kit (#217084, Qiagen), according to the manufacturer's instructions.

RNA sequencing

Total RNA was extracted, and multiplexed libraries were prepared and validated using the Agilent BioAnalyzer, normalized and pooled for sequencing. One nanogram total RNA from each sample was used to prepare sequencing libraries using the SMART-Seq HT (Takara) library prep kit following manufacturer recommended protocol. Each sample library was prepared from cells obtained from at least five pups or two adult mice.

Eleven PCR cycles were used for the cDNA amplification step followed by 12 PCR cycles for the Nextera amplification enrichment. Libraries were then sequenced on an Illumina NextSeq500 sequencer to generate approximately 20 M 75-base single reads for each sample. The reads were trimmed for the adapter sequences using cutadapt 1.18 (Martin 2011) with Python 3.6.3. The trimmed reads were mapped to the mouse reference genome (ENSEMBL build GRCm38 r91) using the STAR aligner 2.5.2a (Dobin et al., 2013). Gene abundance was estimated with python 2.7.11, and HTSeq 0.11.0 (Anders et al., 2015). Final gene counts of all samples including raw counts, normalized counts and the differential gene expression analyses was performed using R 3.5.1, and DESeq2 1.20.0 (Love et al., 2014)(4).Distribution of mapped reads over genome features was obtained for each sample using RSeQC 2.6.4 (Wang et al., 2012).

scRNA-seq analysis

ScRNA-seq data from P1 and adult SMG can be obtained from GSE150327 (Hauser et al., 2020). Computational analysis was performed using R & R Studio software and SEURAT package (Butler et al., 2018). Datasets were generated as described (Hauser et al., 2020) and for this analysis, annotated datasets from P1 and adult glands were imported to SEURAT using the 'readRDS' function. Defining genes were identified using the SEURAT 'FindMarkers' function for specific clusters and exported as tables in Data S1. All statistics were performed using SEURAT pipeline's default statistical test, which is based on non-parameteric Wilcoxon rank sum test. As a measure of significance, adjusted p values of <0.05 were chosen. The interaction analysis was based on identification of ligand-receptor pairs obtained from a large-scale map of cell-cell interactions previously published (Ramilowski et al., 2015). The map was adapted to mouse gene names and ligands and receptors found among the defining genes in SG ionocytes were extracted. Based on these lists, potential interactions were identified using the LigandReceptor script available on GitHub (https://github.com/chiblyaa/LigandReceptor). For both potential pairs for ligands and receptors, matrixes were created using the Matrix package and visualized in chord diagrams using the circlize package (Gu et al., 2014). To highlight some interactions, heatmaps were generated using the Superheat package. Custom R scripts can be obtained upon request. Comparative analysis of SG FGF10^{pos}/ASCL3^{pos} ionocytes and rare pulmonary cell types were based on defining genes. Pulmonary data were obtained from Suppl_table_1_enriched_genes_mouse _reference.csv previously published (Plasschaert et al., 2018).

Ionocyte/epithelial cell progenitor (EPCP) co-culture

Lacrimal glands LGs were dissociated as described (see (Gromova et al., 2017)). Red blood cells were removed by incubation with 25 mL of 1X cold red blood cell lysis buffer (1 L of 10X stock solution, pH 7.3: 89.9 g NH_4Cl, 10.0 g $KHCO_3$, 370.0 mg tetrasodium EDTA). Purified LG cells were collected by centrifugation at 400 × g, resuspended in 100 μg/mL DNase, 5 mM $MgCl_2$ in HBSS (DNase, Sigma-Aldrich, #D-4513; HBSS, Sigma, #H-6648) and incubated for 15–30 min at room temperature. The cells were pelleted at 400 × g, washed in HBSS, resuspended in staining buffer PBE (1× PBS, 0.5% bovine serum albumin, 1 mM EDTA) and counted. Approximately 0.5×10^6 cells were pelleted at 400 × g g for 10 min at 4°C and resuspended in 100 μL of staining buffer with the appropriate conjugated antibody. The following antibodies were used: phycoerythrin (PE) rat anti-mouse Ly-6A/E (Sca1) (# 553336, BD Biosciences); PE-Cy7 rat anti-mouse CD31 (# 561410, BD Biosciences); FITC rat anti-mouse CD34 (catalog no. 553733, BD Biosciences); anti-mouse CD117 (c-Kit) allophycocyanin (APC)-eFluor 780 (catalog no. 47-1171-80, eBioscience; and anti-mouse CD326 (EpCAM) APC (catalog no. 17-5791-80, eBioscience). The cells were stained on ice for 1 h with gentle vortexing every 15–20 min, pelleted as above, and resuspended in 1 mL of cold PBE in FACS tubes.

Flow cytometric analysis and FACS were performed at the TSRI Flow Cytometry Core Facility by using Digital LSRII and FACS Vantage DiVa instruments. Data analyses were performed by using FlowJo software. The main population of cells was determined by forward and side scatter area gating, as well as dead cell exclusion via propidium iodide or 7-aminoactinomycin D. Doublets were excluded via forward scatter area versus width and with side scatter area versus width. Control samples labeled with isotype control antibodies and with a single primary antibody were used to determine the background noise because of nonspecific antibody binding and to establish proper compensation for optimum separation between signals. After analysis of controls and establishment of the gates EPCPs have been sorted out as described (Gromova et al., 2017).

Sorted EPCPs were mixed with sorted SMG TOM^{pos} ionocytes of *Fgf10$^{CreERT2/+}$:R26-tdTomato$^{fl/fl}$* mice in 1:1 proportion and have grown in reaggregated cultures for 7 days as described previously (Gromova et al., 2017). Purified ionocytes and purified EPCPs were used as controls.

Ionocyte/MECs co-culture

Ionocytes were obtained from the FGF10^{CreERT2}:Rosa26^{tdTomato} and MECs from the αSMA-GFP mice by FACS as described above (Zyrianova et al., 2019). Purified ionocytes were plated into the center of each well of a four-well chamber slide coated with a thin layer of Matrigel. When cells attached, a 10 μL of low growth factors Matrigel drop was gently spreaded as a thin layer on a top of attached and placed into cell incubator at 37C for 5–10 min. When gel settled, purified MECs have been plated on a top of Matrigel and cells were grown in the defined medium: high glucose DMEM (Thermo Fisher Scientific, # 11995073) supplemented with 0.1% Lipid-Rich Bovine Serum Albumin (AlbuMAX I, Thermo Fisher Scientific, ##11020), insulin-transferrin-selenium (Thermo Fisher Scientific, #41400-045), human transferrin (40 μg/mL, Thermo Fisher, #0030124SA) and freshly prepared ascorbic acid (150 μg/mL). MEC cultures on the Matrigel without ionocyte were used as controls. Cells were grown for 48 h and stained with the phosphor-histone-3 antibody and DAPI to visualize proliferating cells.

QUANTIFICATION AND STATISTICAL ANALYSIS

To examine the statistical significance of the results, analyses were performed with Prism9 v9.1.2 (GraphPad software Inc, La Jolla, CA) software. Normal distribution of datasets was examined with a Shapiro-Wilk normality test. If data passed normality test, statistical significance between two conditions was assessed with an unpaired t-test and results were represented as mean ± standard deviation (SD). To analyze reaggregate cultures the two-tailed Fisher's exact test has been used. To compare more than two groups, a one-way ANOVA was used for normally distributed data and a Kruskal-Wallis test otherwise. Significant differences are represented as * if p value $p < 0.05$, ** if $p < 0.01$ and *** if $p < 0.001$. Each statistical significance test is detailed in the legend.